



A second-order strain gradient fracture model for the brittle materials with micro-cracks by a multiscale asymptotic homogenization

Zhiqiang Yang¹ · Yipeng Rao² · Yi Sun¹ · Junzhi Cui² · Meizhen Xiang³

Received: 2 November 2022 / Accepted: 31 January 2023 / Published online: 14 March 2023
© The Author(s), under exclusive licence to Springer-Verlag GmbH Germany, part of Springer Nature 2023

Abstract

In this work, applying a second-order multiscale asymptotic homogenization, an effective fracture model is established for the brittle materials with periodic distribution of micro-cracks. The novel second-order strain gradient fracture model based on the multiscale asymptotic technique is rigorously derived without any phenomenological assumptions, and the fourth-, sixth-, and eighth-order effective elastic tensors of the fracture criterions are obtained by the first-order and second-order multiscale unit cell functions. The significant features of the novel model are: (i) the first-order, second-order strain gradient effect and microstructure size ξ included in the fracture criterion and (ii) the strain energy and the Griffith criterion for micro-crack extensions obtained by the high-order multiscale asymptotic homogenization. Finally, the effectiveness of the proposed model is compared with the direct numerical simulations (DNS), experimental data and some typical fracture problems including Mode I crack plate, rectangular plate with two symmetric V-notch and a holed plate are also evaluated. These examples show that the second-order strain gradient fracture model is valid for solving the brittle materials with periodic distribution of micro-cracks.

Keywords Second-order strain gradient · Griffith criterion · Asymptotic homogenization · Brittle fracture

1 Introduction

The damage and fracture problems of materials have been an important issue for many engineering applications, and they should be accurately considered when designing the industrial products. Besides, those materials usually contain a larger number of defects including micro-cracks, pores, and so on [1–3]. In particular, such micro-crack defects are widely existed in the materials with periodic/random distribution, and will affect the macroscopic mechanical properties owing to the strong stress concentration effect near cracks.

As long as the micro-crack propagates, the whole stiffness of materials quickly decreases and the materials will ultimately fracture. Inevitably, in order to correctly analyze the macro performance of the materials with micro-cracks, a more efficient numerical approach and related computational techniques should be established to investigate the damage/fracture behaviors of the materials.

The stress of classical continuum theory in a material point only depends on the strains. As a result, the classical continuum fails to accurately catch the small-scale effect and cannot adequately describe the heterogeneous phenomenon. The generalized nonlocal continuum mechanics based on the classical continuum mechanics are developed to effectively describe scale effects of the materials [4, 5], and the stresses are given through volume integration of strain over a domain with finite size. The nonlocal damage theory which uses an integral formula to consider nonlocal effects through the coupling of damage variables and nonlocal equivalent strains was proposed by Pijaudier-Cabot and Bazant [6]. A lot of nonlocal continuum theories, such as stress gradient [7–9], strain gradient [10–12], hybrid stress–strain gradient [13, 14], modified strain gradient [15, 16] and integral types [17, 18]

✉ Zhiqiang Yang
yangzhiqiang@hit.edu.cn

✉ Meizhen Xiang
xiang_meizhen@iapcm.ac.cn

¹ Department of Astronautic Science and Mechanics, Harbin Institute of Technology, Harbin 150001, China

² LSEC, ICMSEC, Academy of Mathematics and Systems Science, Chinese Academy of Sciences, Beijing 100190, China

³ Laboratory of Computational Physics, Institute of Applied Physics and Computational Mathematics, Beijing 100088, China

theories are introduced to avoid the shortcomings of the classical continuum theory. Especially, owing to the effectiveness for describing the scale effect of materials, the strain gradient theories are developed quickly. As we known, the strain gradient theoretical formulations with microstructure have been studied since the mid-1960s along with the works in [19–21]. Further, strain gradient elastic theories were also developed to analyze the nonlinear mechanical problems. Bassani et al. [22, 23] considered the plasticity strain gradient for the incremental or tangential moduli and kept all the characteristics of traditional J_2 flow theories. Also, this plasticity theory was extended to describe rate-independent plastic deformation and effectively evaluated the creep or visco-plasticity effect [24, 25]. Aifantis [26] established the plasticity theory using extra boundary condition and high-order stress quantity. Fleck and Hutchinson [27–29] introduced a strain gradient theory of plasticity based on the notions of statistical storage and geometrically necessary dislocation. In this theory, Fleck and Hutchinson's works were applicable to the general frameworks of coupled stress theories and needed a single material length scale l . Based on classical crystalline kinematics, Gurtin [30] constructed a single-crystal gradient plastic theory that accounted for geometrically necessary dislocation. Menzel [31] extended a geometrically linear formula of high-order gradient plasticity for single and polycrystalline materials on the basis of the continuum theories of dislocation and incompatibility. Gudmundson [32] presented a theoretical framework that covered a wide range of strain gradient plastic effect for isotropic materials. Liu and co-workers [33–36] developed a multi-resolution continuum theory which typically possesses features at several different scales to predict the failure of heterogeneous materials. Furthermore, considering the damage and fracture problems, the previous strain gradient theories were also applied to analyze the stress and strain fields around crack tips [37–40]. Especially, the fracture criterions or damage evolutions of materials with a larger number of micro-cracks [2, 3, 41, 42] were also calculated by the models having the strain gradient effect.

In addition, when simulating the localization problems with classical continua or lower strain gradient theory, a more accurate solution of the materials with microstructure cannot be effectively obtained or the well-posedness of the mathematical description will lose (see Sluys [43] for an overview). To solve these problems, a high-order strain gradient should be established in the constitutive equations, and the shortcomings of continuum mechanics will be overcome [41, 44, 45]. For this purpose, the second-order strain gradient commonly introduces some auxiliary material parameters which reflects the microstructure characteristics of materials. But, the second-gradient terms are usually assumed rather than obtained from the micro-configuration information of the materials, and this high-order model can be considered

to be phenomenological [27]. However, since the excellent abilities of strain gradient theory in modeling scale relative problems have been fully verified, the determination of higher-order gradient using the multiscale techniques has become an important and hot topic. Bacigalupo and Gambarotta [46, 47] developed a computational homogenization for the second-order strain-gradients and obtained effective expressions for higher-order coefficients in heterogeneous periodic materials. Goda and Ganghoffer [48] established anisotropic first and second-order strain-gradient continuous models of composite materials and structures. Further, Berkache et al. [49] extended the anisotropic first and second-order gradient models for two-dimensional random fiber network using heuristic boundary condition. In Yvonnet et al. [50], a second-order computational homogenization approach was developed to evaluate efficient coefficients of Mindlin's strain gradient models from a local heterogeneous Cauchy linearity material. Babu and Patel [51] proposed a novel non-conforming finite element formula for nanoplate utilizing second-order strain gradient Kirchhoff's plate theories. For the nonlinear elastic problems, the second-order computational homogenizations were also developed to the nonlinear contexts according to the FE² methods in Kouznetsova et al. [52], Kouznetsova et al. [53], Lesicar et al. [54] and Feyel [55]. Amongst these methods introduced in previous works, the very common strategies compute the high-order moduli using the kinematic constraints over the representative volume element (RVE) [56–58].

In addition, another popular method based on the classical homogenization [59–61] is also presented to derive the strain gradient for the materials with periodic configurations. As we know, classical homogenization provides a mathematical framework that the macro homogenized equations can be obtained from the microscopic geometric information and constitutive equations, and it cannot only improve the calculation efficiency, but also maintain the calculation accuracy [59–61]. In the past several decades, various multiscale methods for predicting macroscopic properties were developed in order to increase the computation precision for the classical homogenization, including two-scale convergence methods [62], multiscale finite element methods [63, 64], variational multiscale methods [65, 66] and the heterogeneous multiscale methods [67]. Obviously, these multiscale methods can be summarized as the first-order asymptotic homogenization, and they can effectively resolve several practical problems [62–64]. However, owing to the macroscopic solutions changing rapidly over unit cell (UC) regions, the high-order asymptotic homogenization should be given. Cui et al. [68, 69], Allaire and Habibi [70], Bourgat [71], Gamin and Kroener [72], Bacigalupo [73], Smyshlyayev and Cherednichenko [74] studied the different asymptotic homogenization methods through reconstruction of higher order macro derivatives by postprocessing. Triantafyllidis and Bardenhagen [75]

applied the high-order multiscale homogenization to derive the macro gradient moduli. Smyshlyaev and Cherendichenko [74] established the high-order constitutive equations using the multiscale homogenization techniques based on the variational techniques for the antiplane shear problems. Later, Peerlings and Fleck [76] developed the technique to evaluate the strain gradient moduli for 3D linear elastic problems. Among these methods based on multi-scale asymptotic techniques, the calculation of strain gradient modulus needs to solve the boundary value problems on the unit cells.

However, there is a lack of enough researches on the materials with a large number of micro-crack problems. Also, we have not found any effective second-order strain gradient model to study crack extension of the brittle materials with micro-cracks by the high-order multiscale asymptotic homogenization. Thus, this work will establish a second-order strain gradient constitutive law combined with the multiscale asymptotic homogenization and Griffith fracture criterion for the brittle materials with periodic distribution of micro-cracks. In this model, the strain energy which is different from the energy release rates used in Dascalu et al. [77] and Keita et al. [78] is given through the high-order multiscale asymptotic solutions without any phenomenological assumptions. The new strategies result in a brittle fracture model that involve strain gradient and second-order strain gradient terms, which are missing in the model established in Dascalu et al. [77], Keita et al. [78] and Rao et al. [42].

The outline of the work is in the following. Section 2 introduces the governing equations and second-order strain gradient fracture model for the brittle materials with micro-cracks. In Sect. 3, some typical examples including Mode I crack plate, rectangular plate with two symmetric V-notch and a holed plate are proposed to validate the model. Section 4 gives the conclusion and future research field.

2 Second-order strain gradient fracture model

2.1 Governing equations

An elastic medium with periodic distributions of micro-cracks is illustrated in Fig. 1. ξ is a small parameter denoting the size of a unit cell domain, and L denotes the characteristic size of the macroscopic domain (see Fig. 1). The multiscale homogenization methods assume the separation of scales, i.e., $\xi/L \ll 1$. The micro-cracks of the structure with length l are supposed to be straight, and the damage variable satisfies $d = l/\xi$. $d=0$ indicates the material is not damaged and $d=1$ means the complete fracture. Also, the crack closures are ignored, and the micro-cracks of the brittle materials do not intersect each other.

The domain Ω^ξ , as illustrated in Fig. 1 (a), has the forms: $\Omega^\xi = \Omega \cap \xi\omega$, where Ω is a bounded Lipschitz convex domain without cracks, and ω is a smooth unbounded domain of \mathbf{R}^2 with a 1-periodic structure. The governing equations for the brittle materials are introduced as follows:

$$\begin{aligned}\sigma_{ij}^\xi(\mathbf{x}) &= L_{ijkl}^\xi(\mathbf{x})\varepsilon_{kl}^\xi(\mathbf{x}), & \mathbf{x} \in \Omega^\xi, \\ \varepsilon_{kl}^\xi(\mathbf{x}) &\equiv u_{(k,x_l)}^\xi(\mathbf{x}) = \frac{1}{2} \left[\frac{\partial u_k^\xi(\mathbf{x})}{\partial x_l} + \frac{\partial u_l^\xi(\mathbf{x})}{\partial x_k} \right], & \mathbf{x} \in \Omega^\xi, \\ -\frac{\partial}{\partial x_j} \left[L_{ijkl}^\xi(\mathbf{x})\varepsilon_{kl}^\xi(\mathbf{u}^\xi(\mathbf{x})) \right] &= f_i(\mathbf{x}), & \mathbf{x} \in \Omega^\xi,\end{aligned}\quad (1)$$

where $\mathbf{u}^\xi(\mathbf{x}) = (u_1^\xi(\mathbf{x}), u_2^\xi(\mathbf{x}), u_3^\xi(\mathbf{x}))^T$ are the displacement fields; $\varepsilon^\xi(\mathbf{u}^\xi(\mathbf{x}))$ denote the elastic strains; $\mathbf{f}(\mathbf{x})$ is the body force; $L_{ijkl}^\xi(\mathbf{x}) = L_{ijkl}(\frac{\mathbf{x}}{\xi})$ are the elastic tensors satisfying symmetry

$$L_{ijkl}\left(\frac{\mathbf{x}}{\xi}\right) = L_{jikl}\left(\frac{\mathbf{x}}{\xi}\right) = L_{jilk}\left(\frac{\mathbf{x}}{\xi}\right) = L_{klij}\left(\frac{\mathbf{x}}{\xi}\right),$$

and ellipticity

$$\lambda_1 \eta_{ij} \eta_{ij} \leq L_{ijkl}\left(\frac{\mathbf{x}}{\xi}\right) \eta_{ij} \eta_{kl} \leq \lambda_2 \eta_{ij} \eta_{ij},$$

λ_1 and λ_2 denote the constants satisfying $\eta_{ij} = \eta_{ji}$. We also have $\mathbf{y} = \frac{\mathbf{x}}{\xi}$ with \mathbf{y} denoting the local coordinate, and then the elastic tensors $L_{ijkl}(\frac{\mathbf{x}}{\xi})$ can be rewritten by $L_{ijkl}(\mathbf{y})$. As a result, the single scale differential operator can be replaced by the two-scale differential operator given by:

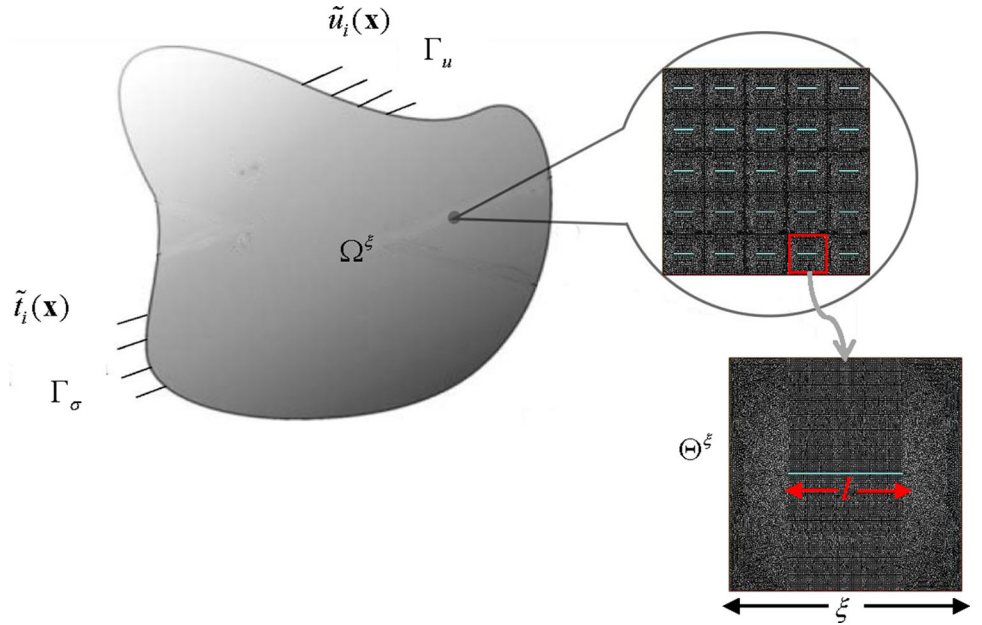
$$\frac{\partial}{\partial x_j} \rightarrow \frac{\partial}{\partial x_j} + \frac{1}{\xi} \frac{\partial}{\partial y_j} \quad (2)$$

The boundary conditions are illustrated as:

$$\begin{aligned}u_i^\xi(\mathbf{x}) &= \bar{u}_i(\mathbf{x}), & \mathbf{x} \in \Gamma_u, \\ v_j L_{ijkl}\left(\frac{\mathbf{x}}{\xi}\right) \left[\varepsilon_{kl}^\xi(\mathbf{u}^\xi(\mathbf{x})) \right] &= \bar{t}_i(\mathbf{x}), & \mathbf{x} \in \Gamma_\sigma, \\ \sigma^\xi(\mathbf{x}) \cdot \mathbf{n} &= 0, [\mathbf{u}^\xi(\mathbf{x}) \cdot \mathbf{n}] > 0, & \mathbf{x} \in \Gamma_\xi^C,\end{aligned}\quad (3)$$

where Γ_u and Γ_σ denote the boundaries of Ω^ξ , and satisfy $\Gamma_u \cup \Gamma_\sigma = \emptyset$, $\Gamma_u \cap \Gamma_\sigma = \partial\Omega$ (see Fig. 1); $\bar{\mathbf{u}}(\mathbf{x})$ and $\bar{\mathbf{t}}(\mathbf{x})$ represent the displacements and tractions on Γ_u and Γ_σ , respectively; \mathbf{n} represent the outward normal vectors on crack surface; $[\cdot]$ denotes the jump across the crack face. Γ_ξ^C are the boundaries that are composed of interior surfaces of micro-cracks $\Gamma_{\xi,m}^C$, such that $\Gamma_\xi^C = \bigcup_{m=1}^{m(\xi)} \Gamma_{\xi,m}^C$, and $m(\xi)$ denote the number of cracks contained in materials. Besides, we have $\partial\Omega^\xi = \partial\Omega \cup \Gamma_\xi^C$.

Fig. 1 The brittle materials with periodic distribution of micro-cracks



2.2 Microscale problems and homogenization problems

Apply the classical asymptotic homogenization [59–61], $u_i^\xi(\mathbf{x})$ have the following forms:

$$u_i^\xi(\mathbf{x}) = u_i^{(0)}(\mathbf{x}) + \xi u_i^{(1)}\left(\mathbf{x}, \frac{\mathbf{x}}{\xi}\right) + \xi^2 u_i^{(2)}\left(\mathbf{x}, \frac{\mathbf{x}}{\xi}\right) + \dots, \quad (4)$$

where $\mathbf{u}^{(0)} = \mathbf{u}^{(0)}(\mathbf{x})$ denotes the homogenized displacement fields. Further, considering the two-scale operators (2) and inserting (4) into (1) yields to the following equalities with different ξ^{-2} , ξ^{-1} and ξ^0 -terms.

$$O(\xi^{-2}): -\frac{\partial}{\partial y_j} \left[L_{ijkl}(\mathbf{y}) \frac{\partial u_k^{(0)}(\mathbf{x})}{\partial y_l} \right] = 0, \quad (5)$$

$$O(\xi^{-1}): -\frac{\partial}{\partial y_j} \left\{ L_{ijkl}(\mathbf{y}) \left[\frac{\partial u_k^{(0)}(\mathbf{x})}{\partial x_l} + \frac{\partial u_k^{(1)}(\mathbf{x}, \mathbf{y})}{\partial y_l} \right] \right\} = 0, \quad (6)$$

$$\begin{aligned} O(\xi^0): & -\frac{\partial}{\partial y_j} \left\{ L_{ijkl}(\mathbf{y}) \left[\frac{\partial u_k^{(1)}(\mathbf{x}, \mathbf{y})}{\partial x_l} + \frac{\partial u_k^{(2)}(\mathbf{x}, \mathbf{y})}{\partial y_l} \right] \right\} \\ & -\frac{\partial}{\partial x_j} \left\{ L_{ijkl}(\mathbf{y}) \left[\frac{\partial u_k^{(0)}(\mathbf{x})}{\partial x_l} + \frac{\partial u_k^{(1)}(\mathbf{x}, \mathbf{y})}{\partial y_l} \right] \right\} = f_i(\mathbf{x}), \end{aligned} \quad (7)$$

Since $u_i^{(0)}(\mathbf{x})$ are independent of \mathbf{y} , it follows that (5) always hold. Utilizing the asymptotic homogenization methods [59, 61], the solutions of (6) should have the following

forms:

$$u_i^{(1)}(\mathbf{x}, \mathbf{y}) = \varphi_i^{kl}(\mathbf{y}) \varepsilon_{kl}^{(0)}(\mathbf{x}), \quad (8)$$

where $\varphi_i^{kl}(\mathbf{y})$ denotes the first-order unit cell function. $\varepsilon_{kl}^{(0)}(\mathbf{x}) \equiv u_{(k, xl)}^{(0)}(\mathbf{x}) = \frac{1}{2} \left[\frac{\partial u_k^{(0)}(\mathbf{x})}{\partial x_l} + \frac{\partial u_l^{(0)}(\mathbf{x})}{\partial x_k} \right]$ are so-called the homogenized strains or coarse-scale strains. Furthermore, substituting (8) into (6), the periodic functions $\varphi_k^{\alpha_1 m}(\mathbf{y})$ should satisfy the following equations:

$$\begin{cases} \frac{\partial}{\partial y_j} \left[L_{ijkl}(\mathbf{y}) \frac{1}{2} \left(\frac{\partial \varphi_k^{\alpha_1 m}(\mathbf{y})}{\partial y_l} + \frac{\partial \varphi_l^{\alpha_1 m}(\mathbf{y})}{\partial y_k} \right) \right] = -\frac{\partial L_{ijm\alpha_1}(\mathbf{y})}{\partial y_j}, & \text{in } \Theta_s, \\ n_i \left(L_{ijkl}(\mathbf{y}) \frac{1}{2} \left(\frac{\partial \varphi_k^{\alpha_1 m}(\mathbf{y})}{\partial y_l} + \frac{\partial \varphi_l^{\alpha_1 m}(\mathbf{y})}{\partial y_k} \right) + L_{ijm\alpha_1}(\mathbf{y}) \right) = 0, \quad \mathbf{y} \in \Gamma^{C\pm}, \\ \varphi_k^{\alpha_1 m}(\mathbf{y}) & \text{is } \Theta - \text{periodic,} \end{cases} \quad (9)$$

where $\Theta_s = \Theta \setminus \Gamma^C$ represents the solid part of the unit cell domain Θ . The upper and lower surfaces of the micro-crack in Θ are denoted as Γ^{C+} and Γ^{C-} , and satisfy $\Gamma^C = \Gamma^{C+} \cup \Gamma^{C-}$.

Integrating average over Θ on (7) and considering (8)–(9), the homogenized equilibrium equations with regard to (1) are obtained:

$$\begin{cases} -\frac{\partial}{\partial x_j} \left[\bar{L}_{ijkl} \frac{1}{2} \left(\frac{\partial u_k^{(0)}(\mathbf{x})}{\partial x_l} + \frac{\partial u_l^{(0)}(\mathbf{x})}{\partial x_k} \right) \right] = \frac{|\Theta_s|}{|\Theta|} f_i(\mathbf{x}), \quad \mathbf{x} \in \Omega, \\ v_j \bar{L}_{ijkl} \frac{1}{2} \left(\frac{\partial u_k^{(0)}(\mathbf{x})}{\partial x_l} + \frac{\partial u_l^{(0)}(\mathbf{x})}{\partial x_k} \right) = \bar{t}_i(\mathbf{x}), \quad \mathbf{x} \in \Gamma_\sigma, \\ u_i^{(0)}(\mathbf{x}) = \bar{u}_i(\mathbf{x}), \quad \mathbf{x} \in \Gamma_u, \end{cases} \quad (10)$$

where \bar{L}_{ijkl} are termed as the homogenized coefficients, and defined by

$$\bar{L}_{ijkl} = \frac{1}{|\Theta|} \int_{\Theta_s} \left[L_{ijkl}(\mathbf{y}) + L_{ijm\alpha_1}(\mathbf{y}) \frac{\partial \varphi_m^{kl}(\mathbf{y})}{\partial y_{\alpha_1}} \right] d\mathbf{y}, \quad (11)$$

It can be seen from (11) that \bar{L}_{ijkl} are only depending on the damage variable d . $|\Theta|$ and $|\Theta_s|$ denotes the measures of the regions Θ and Θ_s , respectively. Owing to $|\Theta|=1$, $|\Theta|$ will be omitted in the following.

Further, considering the macro solutions varying over a unit cell region Θ , the first-order asymptotic formulas cannot effectively capture the microscale information of the materials. Thus, the second-order multiscale formulas need to be established to obtain the enough accurate solutions for the stress and displacement distributions. To satisfy (7), the second-order correctors $\mathbf{u}^{(2)}(\mathbf{x}, \mathbf{y})$ are given by

$$u_i^{(2)}(\mathbf{x}, \mathbf{y}) = \Phi_{ip}^{kl}(\mathbf{y}) \frac{\partial}{\partial x_p} \varepsilon_{kl}^{(0)}(\mathbf{x}) \quad (12)$$

where $\Phi_{ip}^{kl}(\mathbf{y})$ are called as the second-order unit cell functions. Then, taking (12) into (7) and applying the homogenized Eqs. (10), $\Phi_{ip}^{kl}(\mathbf{y})$ should satisfy the following equation:

$$\begin{cases} \frac{\partial}{\partial y_j} \left[L_{ijkl}(\mathbf{y}) \frac{1}{2} \left(\frac{\partial \Phi_{km}^{\alpha_1\alpha_2}(\mathbf{y})}{\partial y_l} + \frac{\partial \Phi_{lm}^{\alpha_1\alpha_2}(\mathbf{y})}{\partial y_k} \right) \right] = \frac{1}{|\Theta_s|} \bar{L}_{i\alpha_1 m \alpha_2} \\ - \frac{\partial}{\partial y_j} [L_{ijk\alpha_2}(\mathbf{y}) \varphi_k^{\alpha_1 m}(\mathbf{y})] - L_{i\alpha_1 m \alpha_2}(\mathbf{y}) - L_{i\alpha_1 k j}(\mathbf{y}) \frac{\partial \varphi_k^{\alpha_2 m}(\mathbf{y})}{\partial y_j}, \quad \text{in } \Theta_s, \\ n_i \left[L_{ijkl}(\mathbf{y}) \frac{1}{2} \left(\frac{\partial \Phi_{km}^{\alpha_1\alpha_2}(\mathbf{y})}{\partial y_l} + \frac{\partial \Phi_{lm}^{\alpha_1\alpha_2}(\mathbf{y})}{\partial y_k} \right) + L_{ijk\alpha_2}(\mathbf{y}) \varphi_k^{\alpha_1 m}(\mathbf{y}) \right] = 0, \quad \mathbf{y} \in \Gamma^{C_\pm} \\ \Phi_{km}^{\alpha_1\alpha_2}(\mathbf{y}) \text{ is } \Theta-\text{periodic}, \end{cases} \quad (13)$$

Finally, combining (8), (10) and (12), the first-order $\mathbf{u}_1^\xi(\mathbf{x})$ and second-order $\mathbf{u}_2^\xi(\mathbf{x})$ multiscale displacement solutions for the original problems (1) are summarized as following:

$$\begin{aligned} \mathbf{u}_1^\xi(\mathbf{x}) &= \mathbf{u}^{(0)}(\mathbf{x}) + \xi \left[\boldsymbol{\varphi}^{kl}(\mathbf{y}) \varepsilon_{kl}^{(0)}(\mathbf{x}) \right], \\ \mathbf{u}_2^\xi(\mathbf{x}) &= \mathbf{u}_1^\xi(\mathbf{x}) + \xi^2 \left[\boldsymbol{\Phi}_p^{kl}(\mathbf{y}) \frac{\partial}{\partial x_p} \varepsilon_{kl}^{(0)}(\mathbf{x}) \right], \end{aligned} \quad (14)$$

In addition, using the two-scale differential operators (2) and multiscale formulas (14), the first-order $\varepsilon_{kl}^{(1)\xi}(\mathbf{x})$ and second-order $\varepsilon_{kl}^{(2)\xi}(\mathbf{x})$ multiscale strain solutions are established by

$$\varepsilon_{kl}^{(1)\xi}(\mathbf{x}) = \varepsilon_{kl}^{(0)}(\mathbf{x}) + u_{(k,y_l)}^{(1)}(\mathbf{x}, \mathbf{y}) + \xi u_{(k,x_l)}^{(1)}(\mathbf{x}, \mathbf{y}), \quad (15)$$

and

$$\varepsilon_{kl}^{(2)\xi}(\mathbf{x}) = \varepsilon_{kl}^{(1)\xi}(\mathbf{x}) + \xi u_{(k,y_l)}^{(2)}(\mathbf{x}, \mathbf{y}) + \xi^2 u_{(k,x_l)}^{(2)}(\mathbf{x}, \mathbf{y}), \quad (16)$$

Similarly, the related multiscale asymptotic expansions of stress are also introduced as follows:

$$\sigma_{ij}^\xi(\mathbf{x}) = \sigma_{ij}^{(0)}(\mathbf{x}, \mathbf{y}) + \xi \sigma_{ij}^{(1)}(\mathbf{x}, \mathbf{y}) + \xi^2 \sigma_{ij}^{(2)}(\mathbf{x}, \mathbf{y}) + \dots \quad (17)$$

Besides, the first-order and second-order stress distributions are obtained according to the corresponding strains constructed with the asymptotic expansions of source Eq. (1).

Remark 2.1 The second-order multiscale approximate solutions are equivalent to the solutions of the problem (1) in $O(\xi)$ -order pointwise sense, as given in Appendix A. It is also the main reason why we should develop the second-order multiscale asymptotic expansion in this work.

2.3 Brittle fracture criterion

In this subsection, we focus on building the fracture criterion, which is accomplished by using the first-order and second-order multiscale asymptotic solutions of (1). At first, the local

strain energy density E based on the unit cell Θ is established in the following forms:

$$E^{(1)} = \frac{1}{2} L_{ijkl}^\xi(\mathbf{x}) \varepsilon_{ij}^{(1)\xi}(\mathbf{x}) \varepsilon_{kl}^{(1)\xi}(\mathbf{x}) \quad (18)$$

and

$$E^{(2)} = \frac{1}{2} L_{ijkl}^\xi(\mathbf{x}) \varepsilon_{ij}^{(2)\xi}(\mathbf{x}) \varepsilon_{kl}^{(2)\xi}(\mathbf{x}) \quad (19)$$

where $E^{(1)}$ and $E^{(2)}$ denote the first-order and second-order strain energy density, respectively.

Further, inserting (15) and (16) into (18) and (19), we can obtain that:

$$\begin{aligned}
E^{(1)} = & \frac{1}{2} L_{ijkl}(\mathbf{y}) \varepsilon_{ij}^{(0)}(\mathbf{x}) \varepsilon_{kl}^{(0)}(\mathbf{x}) \\
& + L_{ijkl}(\mathbf{y}) \varepsilon_{kl}^{(0)}(\mathbf{x}) u_{(i,y_j)}^{(1)}(\mathbf{x}, \mathbf{y}) \\
& + \frac{1}{2} L_{ijkl}(\mathbf{y}) u_{(i,y_j)}^{(1)}(\mathbf{x}, \mathbf{y}) u_{(k,y_l)}^{(1)}(\mathbf{x}, \mathbf{y}) \\
& + \xi L_{ijkl}(\mathbf{y}) \varepsilon_{ij}^{(0)}(\mathbf{x}) u_{(k,x_l)}^{(1)}(\mathbf{x}, \mathbf{y}) \\
& + \xi L_{ijkl}(\mathbf{y}) u_{(k,x_l)}^{(1)}(\mathbf{x}, \mathbf{y}) u_{(i,y_j)}^{(1)}(\mathbf{x}, \mathbf{y}) \\
& + \frac{\xi^2}{2} L_{ijkl}(\mathbf{y}) u_{(i,x_j)}^{(1)}(\mathbf{x}, \mathbf{y}) u_{(k,x_l)}^{(1)}(\mathbf{x}, \mathbf{y})
\end{aligned} \tag{20}$$

and

$$\begin{aligned}
E^{(2)} = & E^{(1)} + \xi L_{ijkl}(\mathbf{y}) u_{(i,y_j)}^{(2)}(\mathbf{x}, \mathbf{y}) \varepsilon_{kl}^{(0)}(\mathbf{x}) \\
& + \xi^2 L_{ijkl}(\mathbf{y}) \varepsilon_{ij}^{(0)}(\mathbf{x}) u_{(k,x_l)}^{(2)}(\mathbf{x}, \mathbf{y}) \\
& + \xi L_{ijkl}(\mathbf{y}) u_{(i,y_j)}^{(2)}(\mathbf{x}, \mathbf{y}) u_{(k,y_l)}^{(1)}(\mathbf{x}, \mathbf{y}) \\
& + \xi^2 L_{ijkl}(\mathbf{y}) u_{(i,x_j)}^{(2)}(\mathbf{x}, \mathbf{y}) u_{(k,y_l)}^{(1)}(\mathbf{x}, \mathbf{y}) \\
& + \xi^2 L_{ijkl}(\mathbf{y}) u_{(i,y_j)}^{(2)}(\mathbf{x}, \mathbf{y}) u_{(k,x_l)}^{(1)}(\mathbf{x}, \mathbf{y}) \\
& + \xi^3 L_{ijkl}(\mathbf{y}) u_{(i,x_j)}^{(1)}(\mathbf{x}, \mathbf{y}) u_{(k,x_l)}^{(2)}(\mathbf{x}, \mathbf{y}) \\
& + \frac{\xi^2}{2} L_{ijkl}(\mathbf{y}) u_{(i,y_j)}^{(2)}(\mathbf{x}, \mathbf{y}) u_{(k,y_l)}^{(2)}(\mathbf{x}, \mathbf{y}) \\
& + \xi^3 L_{ijkl}(\mathbf{y}) u_{(i,y_j)}^{(2)}(\mathbf{x}, \mathbf{y}) u_{(k,x_l)}^{(2)}(\mathbf{x}, \mathbf{y}) \\
& + \frac{\xi^4}{2} L_{ijkl}(\mathbf{y}) u_{(i,x_j)}^{(2)}(\mathbf{x}, \mathbf{y}) u_{(k,x_l)}^{(2)}(\mathbf{x}, \mathbf{y})
\end{aligned} \tag{21}$$

Integrating (21) over Θ^ξ , the total strain energy of the reference cells can be obtained:

$$W^{(2)} = \int_{\Theta^\xi} E^{(2)} d\mathbf{x} \tag{22}$$

Then, taking (21) into (22), the total strain energy $W^{(2)}$ are shown in the following forms:

$$\begin{aligned}
W^{(2)} = & \xi^2 \int_{\Theta_s} L_{ijkl} \varphi_{i,j}^{pq} d\mathbf{y} \varepsilon_{pq}^{(0)} \varepsilon_{kl}^{(0)} \\
& + \xi^3 \int_{\Theta_s} L_{ijkl} \left(\varepsilon_{ij}^{(0)} + \varphi_{i,j}^{pq} \varepsilon_{pq}^{(0)} \right) \varphi_k^{mn} d\mathbf{y} \varepsilon_{mn,l}^{(0)} \\
& + \frac{\xi^2}{2} \int_{\Theta_s} L_{ijkl} d\mathbf{y} \varepsilon_{ij}^{(0)} \varepsilon_{kl}^{(0)} \\
& + \frac{\xi^2}{2} \int_{\Theta_s} L_{ijkl} \varphi_{i,j}^{pq} \varphi_{k,l}^{mn} d\mathbf{y} \varepsilon_{pq}^{(0)} \varepsilon_{mn,l}^{(0)} \\
& + \frac{\xi^4}{2} \int_{\Theta_s} L_{ijkl} \varphi_i^{pq} \varphi_k^{mn} d\mathbf{y} \varepsilon_{pq,j}^{(0)} \varepsilon_{mn,l}^{(0)} \\
& + \xi^4 \left(\int_{\Theta_s} L_{ijkl} \Phi_{kp}^{mn} d\mathbf{y} \varepsilon_{ij}^{(0)} \varepsilon_{mn,pl}^{(0)} \right. \\
& \left. + \int_{\Theta_s} L_{ijkl} \Phi_{ip}^{mn} \varphi_{k,l}^{rs} d\mathbf{y} \varepsilon_{mn,pj}^{(0)} \varepsilon_{rs}^{(0)} \right)
\end{aligned}$$

$$\begin{aligned}
& + \int_{\Theta_s} L_{ijkl} \Phi_{ip,j}^{mn} \varphi_k^{rs} d\mathbf{y} \varepsilon_{mn,p}^{(0)} \varepsilon_{rs,l}^{(0)} \\
& + \frac{\xi^4}{2} \int_{\Theta_s} L_{ijkl} \Phi_{ip,j}^{mn} \Phi_{kq,l}^{rs} d\mathbf{y} \varepsilon_{mn,p}^{(0)} \varepsilon_{rs,q}^{(0)} \\
& + \xi^5 \int_{\Theta_s} L_{ijkl} \varphi_i^{rs} \Phi_{kp}^{mn} d\mathbf{y} \varepsilon_{rs,j}^{(0)} \varepsilon_{mn,pl}^{(0)} \\
& + \xi^3 \int_{\Theta_s} \left(L_{ijkl} + L_{ijrs} \varphi_{r,s}^{kl} \right) \Phi_{ip,j}^{mn} d\mathbf{y} \varepsilon_{mn,p}^{(0)} \varepsilon_{kl}^{(0)} \\
& + \xi^5 \int_{\Theta_s} L_{ijkl} \Phi_{ip,j}^{mn} \Phi_{kq}^{rs} d\mathbf{y} \varepsilon_{mn,p}^{(0)} \varepsilon_{rs,ql}^{(0)} \\
& + \frac{\xi^6}{2} \int_{\Theta_s} L_{ijkl} \Phi_{ip}^{mn} \Phi_{kq}^{rs} d\mathbf{y} \varepsilon_{mn,pj}^{(0)} \varepsilon_{rs,ql}^{(0)}
\end{aligned} \tag{23}$$

In addition, owing to the symmetric and anti-symmetric property for the first-order and second-order unit cell functions (see the detailed proof in Appendix B), we have the following relations:

$$\begin{aligned}
& \xi^3 \int_{\Theta_s} L_{ijkl} \left(\varepsilon_{ij}^{(0)} + \varphi_{i,j}^{pq} \varepsilon_{pq}^{(0)} \right) \varphi_k^{mn} d\mathbf{y} \varepsilon_{mn,l}^{(0)} = 0, \\
& \xi^5 \int_{\Theta_s} L_{ijkl} \varphi_i^{rs} \Phi_{kp}^{mn} d\mathbf{y} \varepsilon_{rs,j}^{(0)} \varepsilon_{mn,pl}^{(0)} = 0, \\
& \xi^5 \int_{\Theta_s} L_{ijkl} \Phi_{ip,j}^{mn} \Phi_{kq}^{rs} d\mathbf{y} \varepsilon_{mn,p}^{(0)} \varepsilon_{rs,ql}^{(0)} = 0.
\end{aligned} \tag{24}$$

Using the (24), (23) can be rewritten by

$$\begin{aligned}
W^{(1)} = & \frac{\xi^2}{2} \int_{\Theta_s} \left(L_{pqkl} + L_{ijkl} \varphi_{i,j}^{pq} \right) d\mathbf{y} \varepsilon_{pq}^{(0)} \varepsilon_{kl}^{(0)} \\
& + \frac{\xi^4}{2} \int_{\Theta_s} L_{ijkl} \varphi_i^{pq} \varphi_k^{mn} d\mathbf{y} \varepsilon_{pq,j}^{(0)} \varepsilon_{mn,l}^{(0)}
\end{aligned} \tag{25}$$

and

$$\begin{aligned}
W^{(2)} = & W^{(1)} + \xi^3 \int_{\Theta_s} \left(L_{ijkl} + L_{ijrs} \varphi_{r,s}^{kl} \right) \Phi_{ip,j}^{mn} d\mathbf{y} \varepsilon_{mn,p}^{(0)} \varepsilon_{kl}^{(0)} \\
& + \xi^4 \int_{\Theta_s} \left(L_{ijrs} + L_{ijkl} \varphi_{k,l}^{rs} \right) \Phi_{ip}^{mn} d\mathbf{y} \varepsilon_{rs,j}^{(0)} \varepsilon_{mn,pj}^{(0)} \\
& + \xi^4 \int_{\Theta_s} L_{ijkl} \Phi_{ip,j}^{mn} \varphi_k^{rs} d\mathbf{y} \varepsilon_{mn,p}^{(0)} \varepsilon_{rs,l}^{(0)} \\
& + \frac{\xi^4}{2} \int_{\Theta_s} L_{ijkl} \Phi_{ip,j}^{mn} \Phi_{kq,l}^{rs} d\mathbf{y} \varepsilon_{mn,p}^{(0)} \varepsilon_{rs,q}^{(0)} \\
& + \frac{\xi^6}{2} \int_{\Theta_s} L_{ijkl} \Phi_{ip}^{mn} \Phi_{kq}^{rs} d\mathbf{y} \varepsilon_{mn,pj}^{(0)} \varepsilon_{rs,ql}^{(0)} = W^{(1)} \\
& + \xi^4 \int_{\Theta_s} \left(L_{ijrs} + L_{ijkl} \varphi_{k,l}^{rs} \right) \Phi_{ip}^{mn} d\mathbf{y} \varepsilon_{mn,pj}^{(0)} \varepsilon_{rs}^{(0)} \\
& + \xi^4 \int_{\Theta_s} L_{ijkl} \Phi_{ip,j}^{mn} \varphi_k^{rs} d\mathbf{y} \varepsilon_{mn,p}^{(0)} \varepsilon_{rs,l}^{(0)} \\
& + \frac{\xi^4}{2} \int_{\Theta_s} L_{ijkl} \Phi_{ip,j}^{mn} \Phi_{kq,l}^{rs} d\mathbf{y} \varepsilon_{mn,p}^{(0)} \varepsilon_{rs,q}^{(0)}
\end{aligned}$$

$$+ \frac{\xi^6}{2} \int_{\Theta_s} L_{ijkl} \Phi_{ip}^{mn} \Phi_{kq}^{rs} d\mathbf{y} \varepsilon_{mn,pj}^{(0)} \varepsilon_{rs,ql}^{(0)} \quad (26)$$

In (25) and (26), $W^{(1)}$ and $W^{(2)}$ denote the first-order and second-order strain energy, respectively. Also, the following equalities are considered to derive the (25) and (26) owing to the symmetric and anti-symmetric property of the first-order and second-order unit cell functions (see the proof in Appendixes B and C)

$$\begin{aligned} \frac{\xi^2}{2} \int_{\Theta_s} (L_{pqkl} + L_{ijkl} \varphi_{i,j}^{pq}) \varphi_{k,l}^{mn} d\mathbf{y} \varepsilon_{pq}^{(0)} \varepsilon_{mn}^{(0)} &= 0, \\ \xi^3 \int_{\Theta_s} (L_{ijkl} + L_{ijrs} \varphi_{r,s}^{kl}) \Phi_{ip,j}^{mn} d\mathbf{y} \varepsilon_{mn,p}^{(0)} \varepsilon_{kl}^{(0)} &= 0. \end{aligned} \quad (27)$$

Furthermore, (26) can be simplified to the equality:

$$\begin{aligned} W^{(2)} = W^{(1)} &+ \xi^4 \left(\bar{C}_{jpmnrs} \varepsilon_{mn,pj}^{(0)}(\mathbf{x}) \varepsilon_{rs}^{(0)}(\mathbf{x}) + \bar{K}_{rsmnpq} \varepsilon_{mn,p}^{(0)}(\mathbf{x}) \varepsilon_{rs,q}^{(0)}(\mathbf{x}) \right) \\ &+ \frac{\xi^6}{2} \bar{F}_{jlrsmnpq} \varepsilon_{mn,pj}^{(0)}(\mathbf{x}) \varepsilon_{rs,ql}^{(0)}(\mathbf{x}) \end{aligned} \quad (28)$$

where

$$\begin{aligned} \bar{K}_{rsmnpq} &= \int_{\Theta_s} L_{ijkq}(\mathbf{y}) \Phi_{ip,j}^{mn}(\mathbf{y}) \varphi_k^{rs}(\mathbf{y}) d\mathbf{y} \\ &\quad + \frac{1}{2} \int_{\Theta_s} L_{ijkl}(\mathbf{y}) \Phi_{ip,j}^{mn}(\mathbf{y}) \Phi_{kq,l}^{rs}(\mathbf{y}) d\mathbf{y}, \\ \bar{C}_{jpmnrs} &= \int_{\Theta_s} (L_{ijrs}(\mathbf{y}) + L_{ijkl}(\mathbf{y}) \varphi_{k,l}^{rs}(\mathbf{y})) \Phi_{ip}^{mn}(\mathbf{y}) d\mathbf{y}, \\ \bar{D}_{pqjml} &= \int_{\Theta_s} L_{ijkl} \varphi_i^{pq}(\mathbf{y}) \varphi_k^{mn}(\mathbf{y}) d\mathbf{y}, \\ \bar{F}_{jlrsmnpq} &= \int_{\Theta_s} L_{ijkl}(\mathbf{y}) \Phi_{ip}^{mn}(\mathbf{y}) \Phi_{kq}^{rs}(\mathbf{y}) d\mathbf{y}. \end{aligned} \quad (29)$$

According to the Griffith criterions for a cell including a crack, the crack will extend as the energy release rate G exceeding a critical value G_c

$$G > G_c \quad (30)$$

Also, the crack propagation is assumed to be straightly along the original directions, and the energy release rate G [42] is evaluated under a quasi-static loading given by:

$$G = - \frac{dW^{(2)}}{dl} \quad (31)$$

Considering $d = l/\xi$, the differential operator has the following forms:

$$\frac{d}{dl} = \frac{1}{\xi} \frac{d}{dd} \quad (32)$$

Then, combining (28), (31) and (32), the energy release rate is given as the functions of the homogenized strain, strain gradient and second-order strain gradient:

$$\begin{aligned} G^{(1)} = - \frac{\xi}{2} \frac{d\bar{L}_{pqkl}}{dd} \varepsilon_{pq}^{(0)}(\mathbf{x}) \varepsilon_{kl}^{(0)}(\mathbf{x}) \\ - \frac{\xi^3}{2} \frac{d\bar{D}_{pqjml}}{dd} \varepsilon_{pq,j}^{(0)}(\mathbf{x}) \varepsilon_{mn,l}^{(0)}(\mathbf{x}) \end{aligned} \quad (33)$$

and

$$\begin{aligned} G^{(2)} = G = G^{(1)} &- \xi^3 \left(\frac{d\bar{C}_{jpmnrs}}{dd} \varepsilon_{mn,pj}^{(0)}(\mathbf{x}) \varepsilon_{rs}^{(0)}(\mathbf{x}) + \frac{d\bar{K}_{rsmnpq}}{dd} \varepsilon_{mn,p}^{(0)}(\mathbf{x}) \varepsilon_{rs,q}^{(0)}(\mathbf{x}) \right) \\ &- \frac{\xi^5}{2} \frac{d\bar{F}_{jlrsmnpq}}{dd} \varepsilon_{mn,pj}^{(0)}(\mathbf{x}) \varepsilon_{rs,ql}^{(0)}(\mathbf{x}) \end{aligned} \quad (34)$$

where $G^{(1)}$ and $G^{(2)}$ represent the first-order and second-order energy release rate, respectively.

Finally, the fracture criterion depending on the small parameter ξ , damage variable d and second-order strain gradient is described by:

$$\begin{aligned} - \frac{\xi}{2} \frac{d\bar{L}_{pqkl}}{dd} \varepsilon_{pq}^{(0)}(\mathbf{x}) \varepsilon_{kl}^{(0)}(\mathbf{x}) - \frac{\xi^3}{2} \frac{d\bar{D}_{pqjml}}{dd} \varepsilon_{pq,j}^{(0)}(\mathbf{x}) \varepsilon_{mn,l}^{(0)}(\mathbf{x}) \\ - \xi^3 \left(\frac{d\bar{C}_{jpmnrs}}{dd} \varepsilon_{mn,pj}^{(0)}(\mathbf{x}) \varepsilon_{rs}^{(0)}(\mathbf{x}) + \frac{d\bar{K}_{rsmnpq}}{dd} \varepsilon_{mn,p}^{(0)}(\mathbf{x}) \varepsilon_{rs,q}^{(0)}(\mathbf{x}) \right) \\ - \frac{\xi^5}{2} \frac{d\bar{F}_{jlrsmnpq}}{dd} \varepsilon_{mn,pj}^{(0)}(\mathbf{x}) \varepsilon_{rs,ql}^{(0)}(\mathbf{x}) > G_c \end{aligned} \quad (35)$$

From (35), it can be seen that the coefficients of the fracture criterion are given by the derivatives of effective elasticity tensors \bar{L}_{pqkl} , \bar{D}_{pqjml} , \bar{C}_{jpmnrs} , \bar{K}_{rsmnpq} and $\bar{F}_{jlrsmnpq}$ about the normalized damage variable d , which are evaluated according to the first-order and second-order unit cell functions introduced in (29). The fracture criterion is established in this work based on the strain energy density [42] which is different from the Dascalu et al. [77]’ work. In addition, if the strain gradient and second-order strain gradient terms are ignored for the new model, the fracture criterion (35) established in this work will change to the model given by Dascalu et al. [77]. Also, if the second-order strain gradient terms are ignored for the new model, the fracture criterion (35) will change to the model provided by Rao et al. [42].

3 Numerical examples and discussions

3.1 Effective materials properties

In this subsection, the effective coefficients of (29) including \bar{L}_{pqkl} , \bar{D}_{pqjmn} , \bar{C}_{jpmnrs} , \bar{K}_{rsmnpq} and $\bar{F}_{jlrsmnpq}$ are firstly computed for 199 values in the interval $d \in (0, 1)$ with uniform distributions. Further, the effective coefficients and the derivatives of the coefficients are obtained by the cubic spline interpolation for any d (micro-crack length at a unit cell). Finally, considering the actual computations, a macroscopic point of the homogenized structure is fractured if $G > G_c$. For this example, we choose the Young's modulus $E = 2\text{GPa}$, Poisson ratio $\nu = 0.3$ and fracture energy $G_c = 1\text{J/m}^2$. The brittle materials with periodic micro-cracks are considered, and the first-order $\varphi^{kl}(\mathbf{y})$ and second-order $\Phi_p^{kl}(\mathbf{y})$ multiscale functions are evaluated by the triangular mesh with refined near the tips of crack, as shown in Appendix B. Obviously, the unit cell solution is symmetric or anti-symmetric about the axe which is parallel or vertical to the crack. In addition, the proof of symmetric or anti-symmetric features for the unit cell functions are also given in Appendix B.

Owing to the symmetry of $L_{ijkl}(\mathbf{y})$, $\varphi_i^{kl}(\mathbf{y})$ and $\Phi_i^{kl}(\mathbf{y})$, the effective coefficients satisfy $\bar{D}_{pqjmn} = \bar{D}_{qpjmn} = \bar{D}_{qpjnm} = \bar{D}_{mnlpq}, \bar{K}_{rsmnpq} = \bar{K}_{srsmnpq} = \bar{K}_{rsnmpq}, \bar{C}_{jpmnrs} = \bar{C}_{jpmnrs} = \bar{C}_{jpmnsr}$ and $\bar{F}_{jlrsmnpq} = \bar{F}_{jlsrmnpq} = \bar{F}_{jlrsmnpq} = \bar{F}_{jlmnrsqp}$. According to the symmetric or anti-symmetric property for the first-order and second-order unit cell functions, the sixth-order tensor \bar{D}_{pqjmn} have 12 non-zero values, \bar{K}_{rsmnpq} have 18 non-zero values and \bar{C}_{jpmnrs} have 18 non-zero values. The eighth-order tensor $\bar{F}_{jlrsmnpq}$ have 42 non-zero values. Figure 2 illustrates the coefficients of \bar{L}_{pqkl} and \bar{D}_{pqjmn} as a function

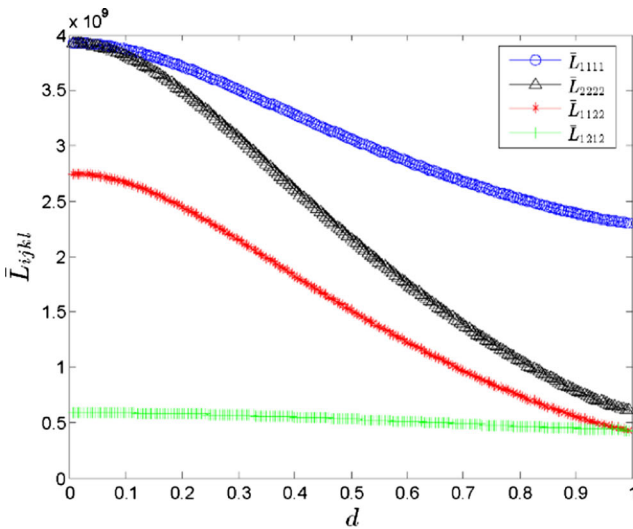


Fig. 2 **a** Curve of \bar{L}_{pqkl} as a function d ; **b** curve of \bar{D}_{pqjmn} as a function d

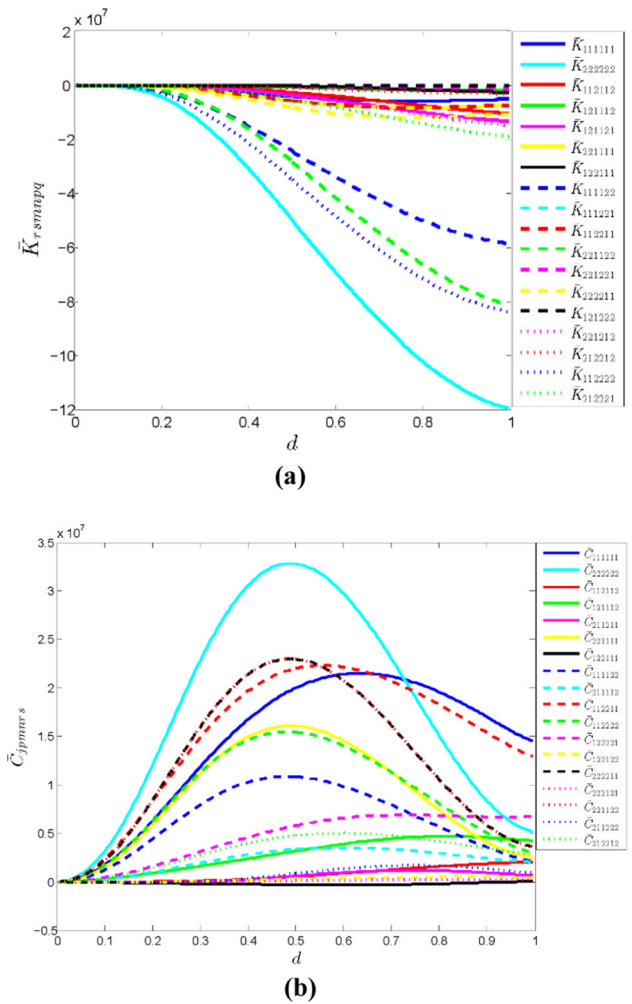


Fig. 3 **a** Curve of \bar{K}_{rsmnpq} as a function d ; **b** curve of \bar{C}_{jpmnrs} as a function d

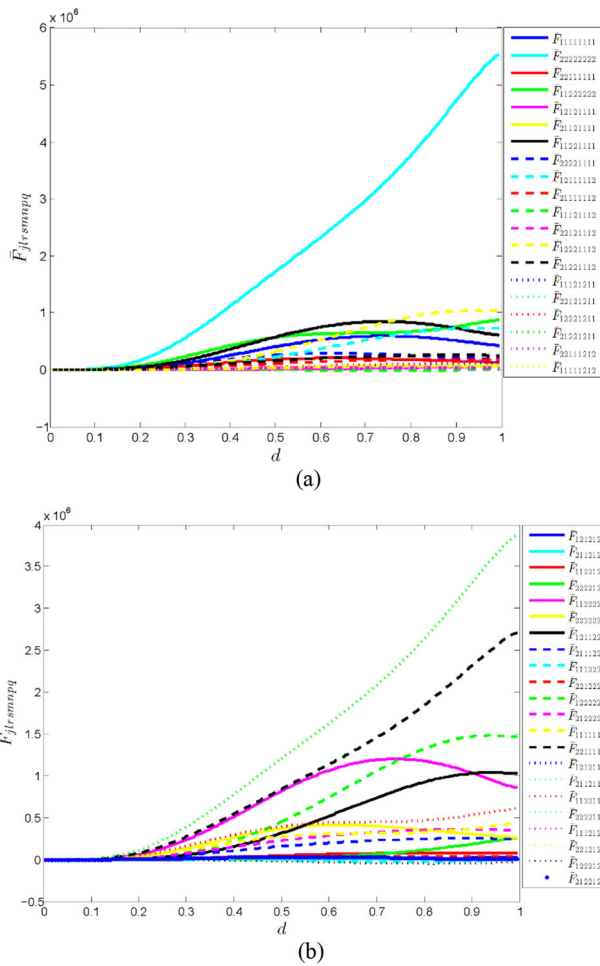


Fig. 4 Curve of $\bar{F}_{jlrsmpq}$ as a function d

of normalized crack length d , and the curves are similar with the values provided in Rao et al. [42]. Figures 3 and 4 illustrates the coefficients of \bar{K}_{rsmpq} , \bar{C}_{jpmnrs} and $\bar{F}_{jlrsmpq}$ as a function of d . As a result, \bar{K}_{rsmpq} are all decreasing as d increasing from 0 to 1, and most $\bar{F}_{jlrsmpq}$ are increasing as d increasing. \bar{C}_{jpmnrs} are increased at first and then decreased with the varying of d .

Further, a material point of the homogenized structure under uniaxial tensions having only one non-zero strain $\varepsilon_{22}^{(0)}(\mathbf{x})$, only one non-zero strain gradient $\varepsilon_{22,2}^{(0)}(\mathbf{x})$ and second-order strain gradient $\varepsilon_{22,22}^{(0)}(\mathbf{x})$ are considered to analyze the macro effective performance of the materials. In addition, the stress that satisfies the fracture criterion $G = G_c$ is called as critical loading stress (or critical stress or fracture strength, marked by σ_c). Figure 5 shows the σ_c as a function of the microscale size ξ for different normalized micro-crack d , and the $\varepsilon_{22,2}^{(0)}(\mathbf{x}) = 0$ and $\varepsilon_{22,22}^{(0)}(\mathbf{x}) = 0$. As a result, σ_c is decreased when the ξ is increased, and the critical stress σ_c is increased as the micro-crack d decreasing from 0.5 to 0.1.

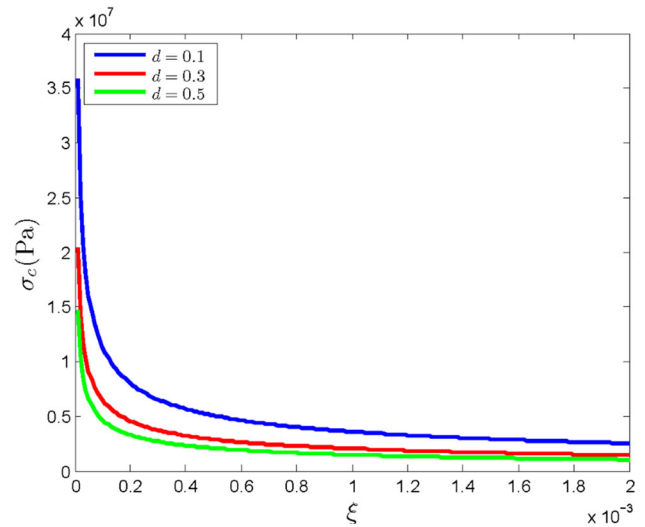


Fig. 5 Fracture strength as a function of ξ , for $d = 0.1, d = 0.3$ and $d = 0.5$

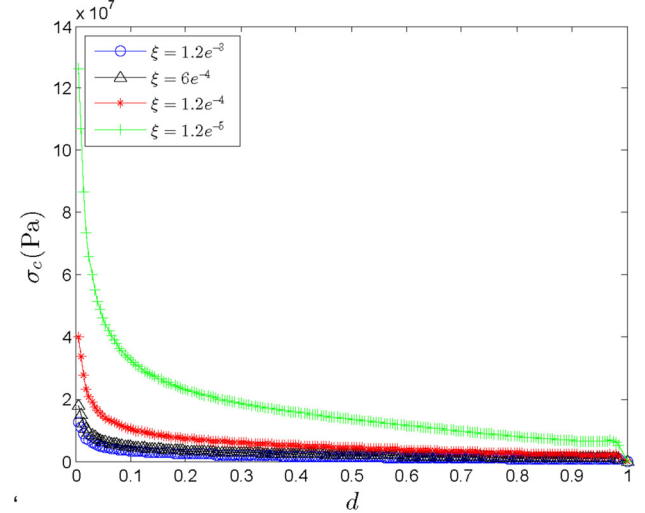


Fig. 6 σ_c as a function of d for various ξ

Figure 6 illustrates the σ_c as a function of the micro-crack d for various ξ , and the $\varepsilon_{22,2}^{(0)}(\mathbf{x}) = 0$ and $\varepsilon_{22,22}^{(0)}(\mathbf{x}) = 0$. The σ_c is decreased when the d is increased, and σ_c is increased when the ξ is decreased. Besides, the critical stress σ_c of brittle material vary rapidly when the micro-crack length d is closed to 0.

Figure 7 illustrates the σ_c as a function of the $\varepsilon_{22,2}^{(0)}(\mathbf{x})$ for the fracture criterion $G^{(1)}$ and the $G^{(2)}$, and the $d = 0.5, \xi = 1e-3$ and $\varepsilon_{22,22}^{(0)}(\mathbf{x}) = 0$. The critical stress σ_c is increased as the $\varepsilon_{22,2}^{(0)}(\mathbf{x})$ is increased, and σ_c for the solutions given by the fracture criterion $G^{(1)}$ is higher than the solutions obtained by the fracture criterion $G^{(2)}$ at $d = 0.5$ and $\xi = 1e-3$. In addition, the fracture criterion $G^{(1)}$ considered the strain gradient have been also discussed in Rao et al. [42]. However,

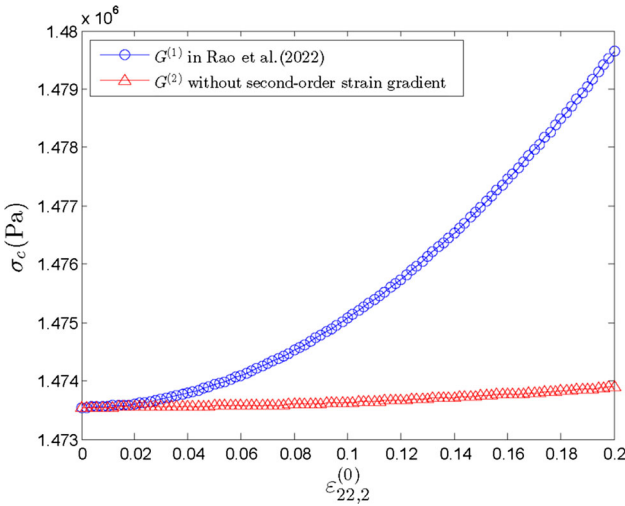


Fig. 7 σ_c as a function of strain gradient $\varepsilon_{22,2}^{(0)}(\mathbf{x})$ with $d = 0.5$, $\varepsilon_{22,22}^{(0)} = 0$ and $\xi = 1e-3$

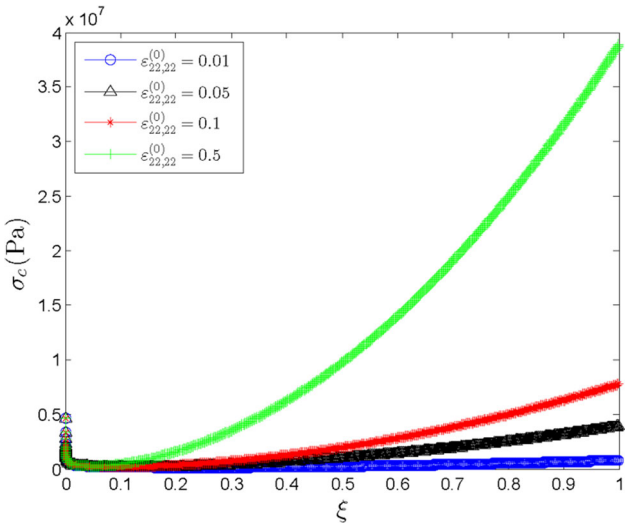


Fig. 8 σ_c as the functions of ξ for distinct $\varepsilon_{22,22}^{(0)}(\mathbf{x})$ with $d = 0.5$ and $\varepsilon_{22,2}^{(0)} = 0$

the strain gradient term $\xi^3 \frac{d\bar{K}_{rsmpq}}{dd} \varepsilon_{mn,p}^{(0)}(\mathbf{x}) \varepsilon_{rs,q}^{(0)}(\mathbf{x})$ is absent in Rao et al. [42] even if they establish the strain gradient fracture model.

Figure 8 shows the critical stress σ_c as a function of the small parameter ξ for the different second-order strain gradient $\varepsilon_{22,22}^{(0)}(\mathbf{x})$ ($d = 0.5$ and $\varepsilon_{22,2}^{(0)}(\mathbf{x}) = 0$). The critical stress σ_c is decreased as the ξ is increased ($\xi < 1e-4$), and σ_c is increased as the ξ is increased ($\xi > 1e-4$) at $d = 0.5$ and $\varepsilon_{22,2}^{(0)} = 0$. Meanwhile, the critical stress σ_c increases rapidly as the second-order strain gradient $\varepsilon_{22,22}^{(0)}(\mathbf{x})$ is increased ($\xi > 1e-4$), and the σ_c is almost same for the different $\varepsilon_{22,22}^{(0)}(\mathbf{x})$ when $\xi \leq 1e-4$.

Figure 9(a) show the critical stress σ_c as a function of second-order strain gradient $\varepsilon_{22,22}^{(0)}(\mathbf{x})$ for different strain gradient $\varepsilon_{22,2}^{(0)}(\mathbf{x})$ ($d = 0.5$ and $\xi = 0.1$). The critical stress σ_c increase slowly as the $\varepsilon_{22,22}^{(0)}(\mathbf{x})$ is increased ($d = 0.5$ and $\xi = 0.1$), and σ_c is increased rapidly as the increasing of $\varepsilon_{22,2}^{(0)}(\mathbf{x})$ for the same second-order strain gradient $\varepsilon_{22,22}^{(0)}(\mathbf{x})$. Figure 9(b) show the critical stress σ_c as a function of strain gradient $\varepsilon_{22,2}^{(0)}(\mathbf{x})$ for different second-order strain gradient $\varepsilon_{22,22}^{(0)}(\mathbf{x})$ with the $d = 0.5$ and $\xi = 0.1$. The critical stress σ_c increases as the $\varepsilon_{22,2}^{(0)}(\mathbf{x})$ is increased, and σ_c increases as the increasing of $\varepsilon_{22,22}^{(0)}(\mathbf{x})$ for the same strain gradient $\varepsilon_{22,2}^{(0)}(\mathbf{x})$. Obviously, from the Fig. 9, the σ_c of brittle materials are more sensitive to the first-order strain gradient $\varepsilon_{22,2}^{(0)}(\mathbf{x})$ and second-order strain gradient $\varepsilon_{22,22}^{(0)}(\mathbf{x})$ (when $\varepsilon_{22,22}^{(0)}(\mathbf{x}) > 1$) at $d = 0.5$ and $\xi = 0.1$.

3.2 Brittle fracture for macroscopic structures

3.2.1 Effectiveness of the second-order multiscale methods

For the first example, the structures with periodic configurations are illustrated in Fig. 10(a), and the reference cell Θ is given in Fig. 10(b). we also have the $d = 0.5$, $\xi = 1/10$, $f_2(\mathbf{x}) = 1 \times 10^6$ Pa/m and $\bar{\mathbf{u}}(\mathbf{x}) = (0, 0)^T$ for all the boundaries. The mechanical parameters of matrix are $E = 2 \times 10^6$ Pa and $\nu = 0.2$. The linear triangular elements are considered for this example.

In addition, in order to verify the effectiveness of the second-order multiscale displacement (14), we consider the direct numerical simulation (DNS) solutions \mathbf{u}_{DNS} for the original problem (1) as a reference solution. The FE meshes including 332,701 nodes and 658,000 elements for the DNS are adopted. The unit cell meshes consider 3288 nodes and 6316 elements, and five FE meshes are considered for the homogenized models, composing of 8, 50, 200, 800 and 5000 elements, respectively.

The relative errors are obtained by the homogenized, first-order and second-order multiscale displacement solutions about the DNS are studied, i.e. $\text{error}_0 = \mathbf{u}_{\text{DNS}} - \mathbf{u}^{(0)}(\mathbf{x})$, $\text{error}_1 = \mathbf{u}_{\text{DNS}} - \mathbf{u}_1^\xi(\mathbf{x})$, $\text{error}_2 = \mathbf{u}_{\text{DNS}} - \mathbf{u}_2^\xi(\mathbf{x})$ in L^2 and H^1 -norms introduced by.

$$\|v\|_{L^2(\Omega)} = (\int_{\Omega} |v|^2 dx)^{1/2}, \quad \|v\|_{H^1(\Omega)} = (\int_{\Omega} (|\nabla v|^2) dx)^{1/2}$$

The relative errors in the L^2 and H^1 -norms for the three methods are shown in Tables 1, 2, Figs. 11 and 12, respectively.

Figure 13 displays the numerical results for the first component of displacement solutions $\mathbf{u}^\xi(\mathbf{x})$ by the different numerical methods, i.e., homogenized methods, first-order multiscale methods, second-order multiscale methods and

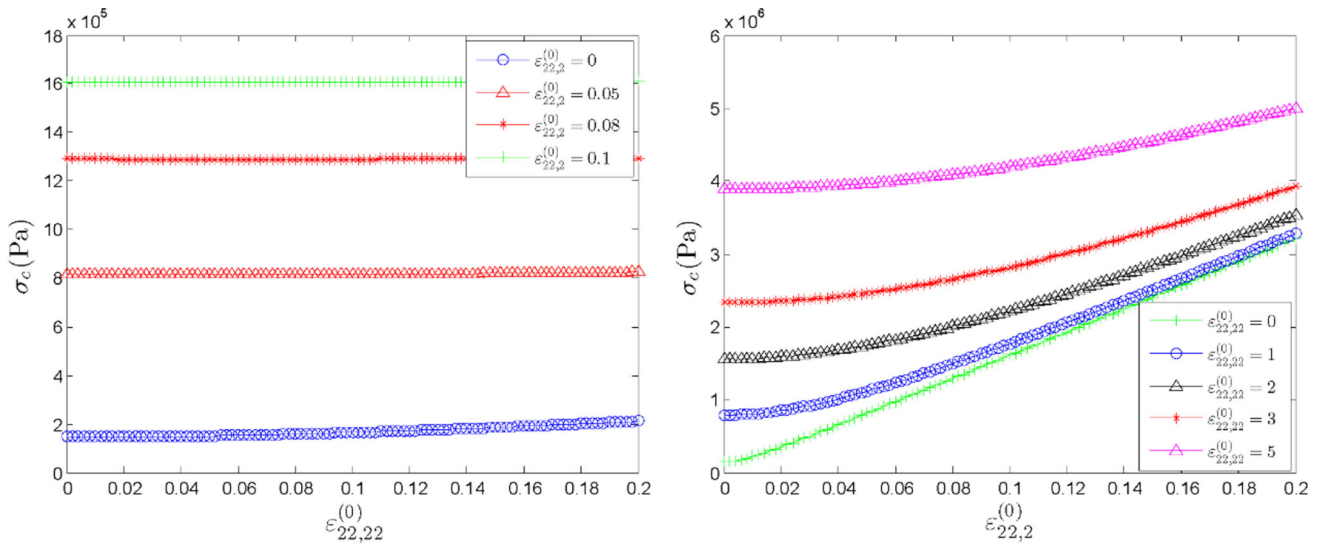


Fig. 9 **a** σ_c as the function of $\varepsilon_{22,22}^{(0)}(\mathbf{x})$ for various $\varepsilon_{22,2}^{(0)}(\mathbf{x})$, and **b** σ_c as the function of for various $\varepsilon_{22,22}^{(0)}(\mathbf{x})$ with $d = 0.5$ and $\xi = 0.1$

Fig. 10 **a** Domain Ω^ξ ; **b** Unit cell $\Theta = [0, 1]^2$

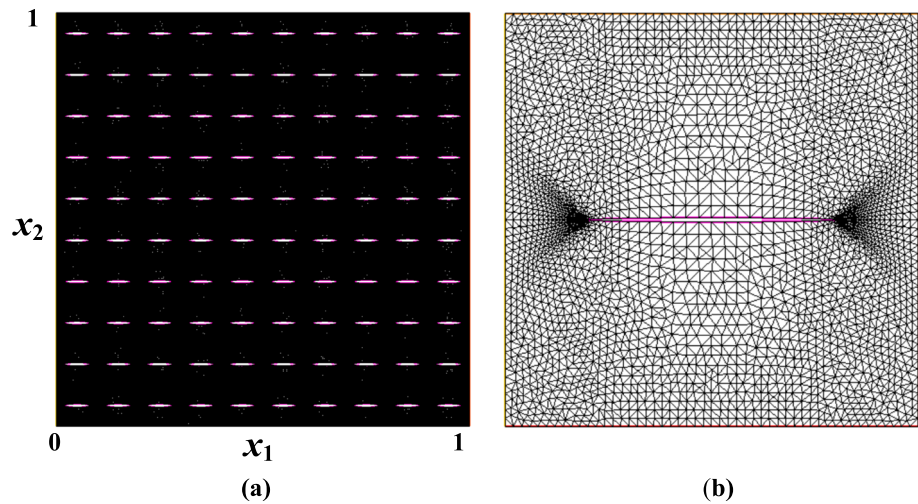


Table 1 Computational results for the three models at norm L^2

	$\ error_0\ _{L^2} / \ u_{\text{DNS}}\ _{L^2}$	$\ error_1\ _{L^2} / \ u_{\text{DNS}}\ _{L^2}$	$\ error_2\ _{L^2} / \ u_{\text{DNS}}\ _{L^2}$
$\xi = 1/10$	0.0513779	0.010982619	0.00889013671

DNS. Figure 14 shows the numerical results for the strain distributions $\boldsymbol{\varepsilon}^\xi(\mathbf{x})$. As a result, from the Tables 1, 2 and Figs. 11, 12, 13, 14, it is found that the homogenization solutions cannot give the better approximation for the DNS, but the second-order multiscale solutions are in good agreement with DNS and can effectively get local information of the periodic materials with micro-cracks.

Also, the second-order multiscale models and the DNS are calculated on the same computers (which possess memory of 8 GB and 4 processors having CPU = 2.71 GHz) by the FreeFem ++ software. It is easy to compute the problems (it needs about 5 s to solve the first-order and second-order unit cell problems, and about 4 s for the homogenization problems with 5000 FE elements). In addition, it takes about 80 s to

Table 2 Computational results for the three models at semi-norm H^1

	$ error_0 _{H^1} / u_{\text{DNS}} _{H^1}$	$ error_1 _{H^1} / u_{\text{DNS}} _{H^1}$	$ error_2 _{H^1} / u_{\text{DNS}} _{H^1}$
$\xi = 1/10$	0.656311	0.244632	0.2136585

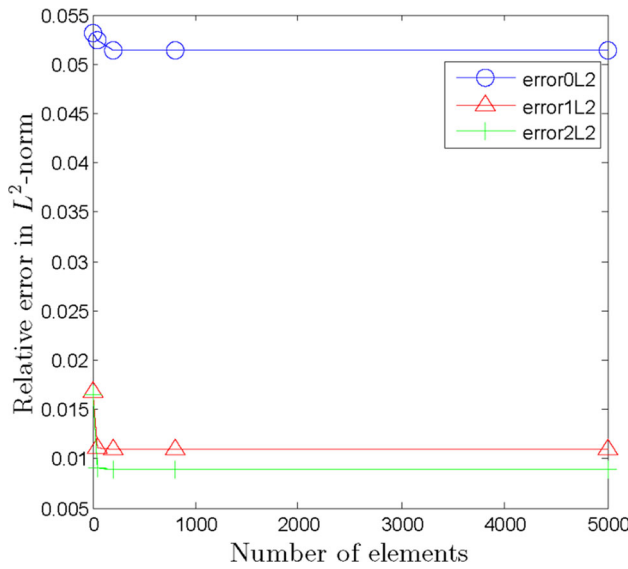


Fig. 11 Relative errors in L^2 -norms for the three models with $\xi = 1/10$

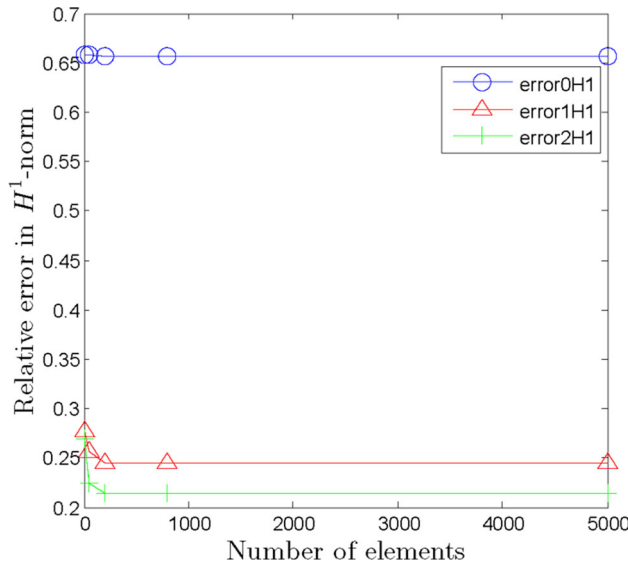


Fig. 12 Relative errors in H^1 -norms for the three models with $\xi = 1/10$

evaluate the multiscale problems by the DNS. Obviously, the presented multiscale models are effective to save CPU time.

3.2.2 Mode I cracked plate

In the following, some representative examples are given to investigate the brittle fracture of macro structures under quasi-static loading. Besides, in order to compute the first-order and second-order strain gradients, the Lagrangian P_3 elements are applied for the displacement interpolations by the triangle meshes. At the beginning of the computation, the strain, first-order and second-order strain gradients at the centroid of each element are calculated. And, for each loading

steps, the iteration is performed to obtain a convergent solution. Further, the energy release rate G (35) is analyzed, and the elements are regarded as fractured (if $G > G_c$). Finally, the numerical simulations will stop when the whole plate structure breaks.

In this example, a rectangular plate having a V-notch with depth $b = 0.01$ m and span $a = 0.001$ m is illustrated in Fig. 15. The length and width of the plate are 0.1 m and 0.05 m, respectively. The FE meshes including 6149 nodes and 11,978 elements for the macro-structure are considered (partitioned numbers along plate boundary are 50 and 100). The material parameters are the same with that given in previous Sect. 3.1, the body force is 0 and the displacement increment is $\Delta u = 5e-7$ m for each loading step of the plate, as demonstrated in Fig. 15.

Figure 16 shows the fracture zone distributions for different fracture criterions based on (35) at initial crack length $d = 0.1$ and $\xi = 1e - 3$. Obviously, the models considering the second-order strain gradient terms result in a wider fracture zone around the centerline (Fig. 16c), and the models considering the strain gradient term and strain term have the same fracture zone with narrow region, as shown in Fig. 16a and b. Figures 16, 17 and 18 show the fracture zone distributions for different fracture criterions at various initial crack length i.e., $d = 0.1$, $d = 0.15$, $d = 0.2$ and $\xi = 1e - 3$. As a result, the fracture zone considering the second-order strain gradient is wider than the fracture zone calculated using the first-order strain gradient and strain terms. Figure 19 shows the fracture zone distributions for different fracture criterions at initial crack length $d = 0.1$ and $\xi = 1e - 4$. It is shown that the fracture zones evaluated by the different fracture criterions have the same area for the parameter $\xi = 1e - 4$, and the results are in accordance with the results as displayed in Fig. 8.

Figure 20 shows the fracture zone based on the second-order fracture criterions $G^{(2)}$ (34) for different meshes at $d = 0.1$ and $\xi = 1e - 4$. The rectangular plate having a V-notch with depth $b = 0.005$ m and span $a = 0.001$ m is considered in Fig. 15. It is found that the fracture zone analyzed using the different meshes is similar (47,918 elements and 107,866 elements). The fracture zone obtained from the fined meshes 47,918 elements and 107,866 elements has little differences, demonstrating a lower mesh sensitivity for the fracture zone using the meshes.

Table 3 shows the fracture strength for the different parameters ξ and fracture criterions at initial micro-crack length $d = 0.1$. $\sigma_c^{(0)}$ denote the fracture strength only considering the strain terms; $\sigma_c^{(1)}$ are the fracture strength based on energy release rate $G^{(1)}$; $\sigma_c^{(2)}$ denote the fracture strength obtained based on the fracture criterions (35). From Table 3, the $\sigma_c^{(0)}$, $\sigma_c^{(1)}$ and $\sigma_c^{(2)}$ are increased as ξ is decreased, and $\sigma_c^{(0)} < \sigma_c^{(1)}$, $\sigma_c^{(1)}$ is slightly less than $\sigma_c^{(2)}$. These results are also in accordance with the macro properties analysis in Sect. 3.1.

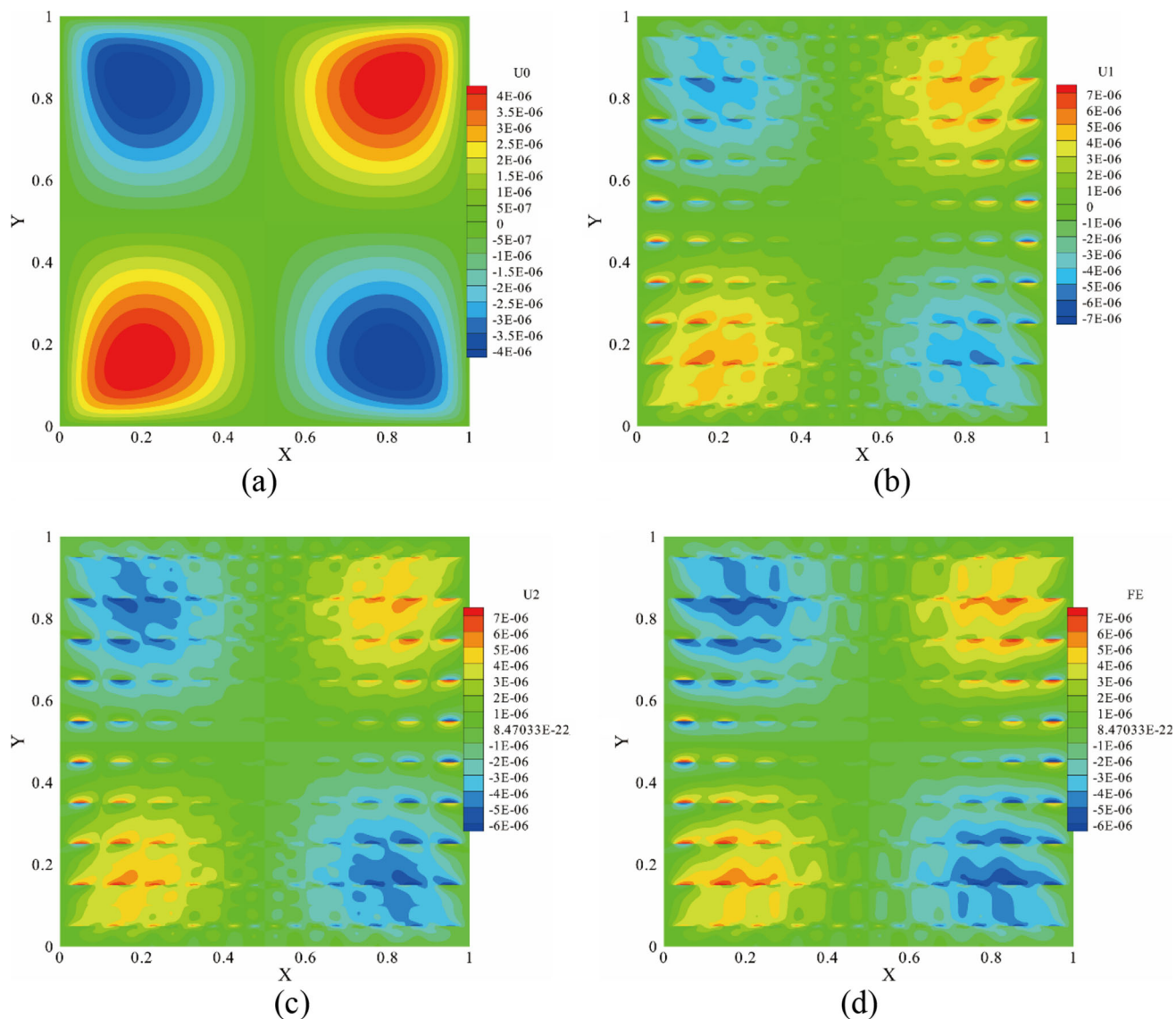


Fig. 13 The first component of the displacement function **a** $\mathbf{u}^{(0)}(\mathbf{x})$; **b** $\mathbf{u}_1^\xi(\mathbf{x})$; **c** $\mathbf{u}_2^\xi(\mathbf{x})$; **d** \mathbf{u}_{DNS}

3.2.3 Rectangular plate with two symmetric V-notch

In this example, a rectangular plate having two symmetric V-notch denoted by depth b and span a is shown in Fig. 21. The length and width of the plate are also 0.1 m and 0.05 m, respectively. The FE meshes including 24,565 nodes and 48,504 elements for the macro-structure are considered (partitioned numbers along the plate boundary are 100 and 200). The material parameters and displacement increment for each loading step of the plate are also the same with that given in previous Sect. 3.2.2.

Figure 22 displays the fracture zone on the basis of different fracture criterions (34) having depth $b = 0.015$ m and span $a = 0.0005$ m at initial crack length $d = 0.1$ and $\xi = 1e - 3$. From the result, we can see that the fracture criterions with

the second-order strain gradient terms have a wider fracture zone around the centerline (Fig. 22c) than the models considering the strain term and first-order strain gradient term (Fig. 22a and b). In short, the fracture zones calculated by the fracture criterions (35) with second-order strain gradient terms are much more dispersed than that without considering second-order strain gradient terms.

Figure 23 displays the fracture zone for different fracture criterions with depth $b = 0.003$ m and span $a = 0.00035$ m at initial length $d = 0.1$ and $\xi = 1e - 4$. Obviously, the fracture zones computed by the different fracture criterions also have the same area for this example at $\xi = 1e - 4$, and the results are also in accordance with the results as given in Fig. 8 and the work introduced in Dascalu et al. [77].

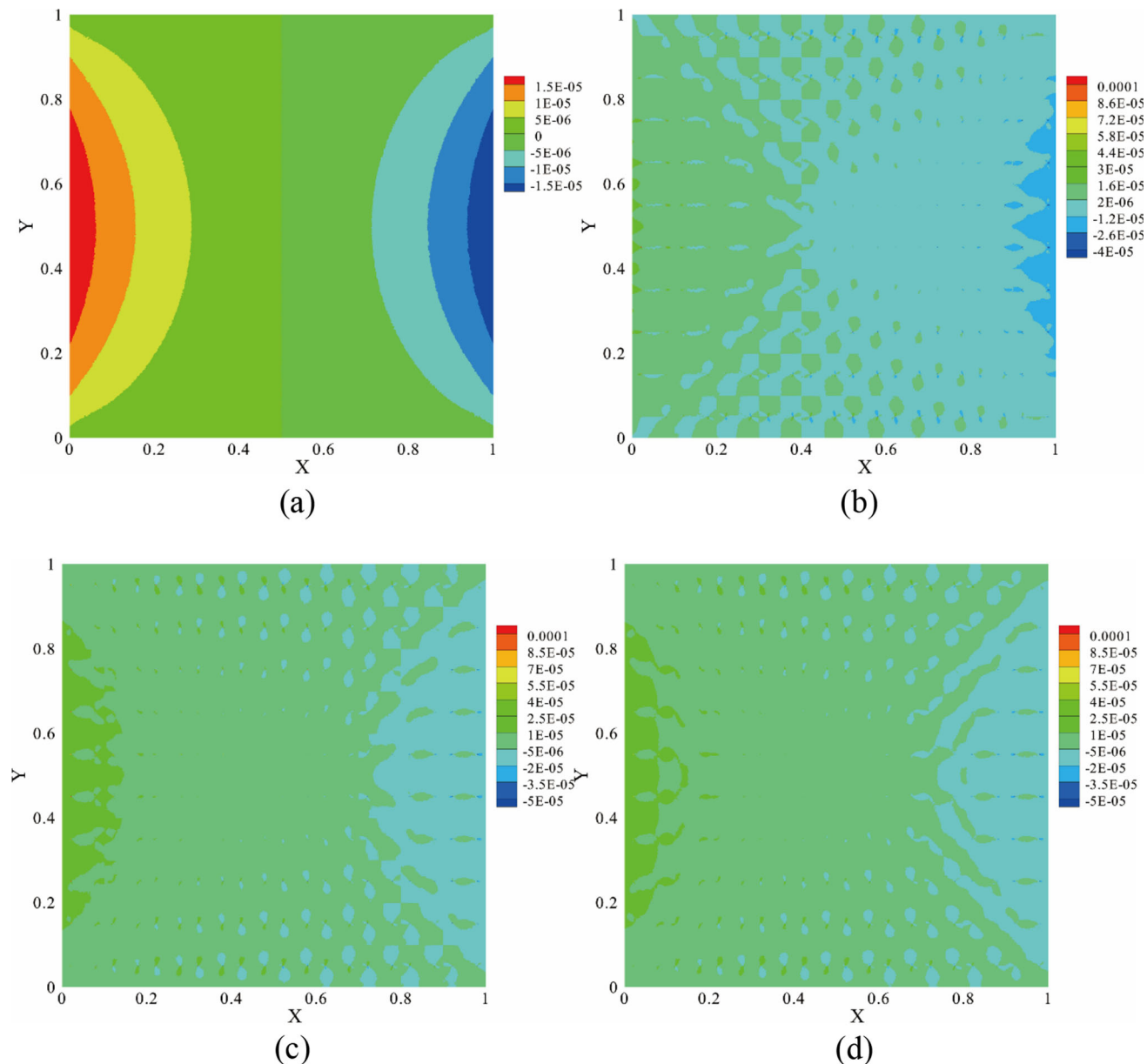


Fig. 14 Strain distributions: **a** $\bar{\varepsilon}_{12}^{\xi}(\mathbf{u}^{(0)}(\mathbf{x}))$; **b** $\bar{\varepsilon}_{12}^{\xi}(\mathbf{u}_1^{\xi}(\mathbf{x}))$; **c** $\bar{\varepsilon}_{12}^{\xi}(\mathbf{u}_2^{\xi}(\mathbf{x}))$; **d** $\bar{\varepsilon}_{12}^{\xi}(\mathbf{u}_{UDNS})$

Figure 24 displays the fracture zone based on the fracture criterions (35) with second-order strain gradient terms for different initial lengths, i.e., $d = 0.2$, $d = 0.6$, $d = 0.8$ and $\xi = 1e - 4$. The depth b and span a of the plate are also 0.003 m and 0.00035 m, respectively. It can be seen from Fig. 24 that the fracture zone is increasing as the increasing of the micro-crack length d .

Figure 25 illustrates the fracture zone on the basis of the fracture criterions $G^{(2)}$ with the second-order strain gradient terms for different meshes at $d = 0.1$ and $\xi = 1e - 4$. It is demonstrated that the fracture zone studied using the different meshes is similar (48,504 elements and 94,578 elements). The fracture zone based on the fined meshes 48,504 elements

and 94,578 elements has little differences, which also shows that the fracture zone using the fined meshes has a lower mesh sensitivity.

Table 4 illustrates the fracture strengths for the different microstructure ξ and fracture criterions at $d = 0.1$. As a result, the $\sigma_c^{(0)}, \sigma_c^{(1)}$ and $\sigma_c^{(2)}$ are also increased as ξ is decreased, and $\sigma_c^{(0)} < \sigma_c^{(1)}, \sigma_c^{(1)}$ is also slightly less than $\sigma_c^{(2)}$. These results are again in accordance with the macro properties analysis in Sect. 3.1.

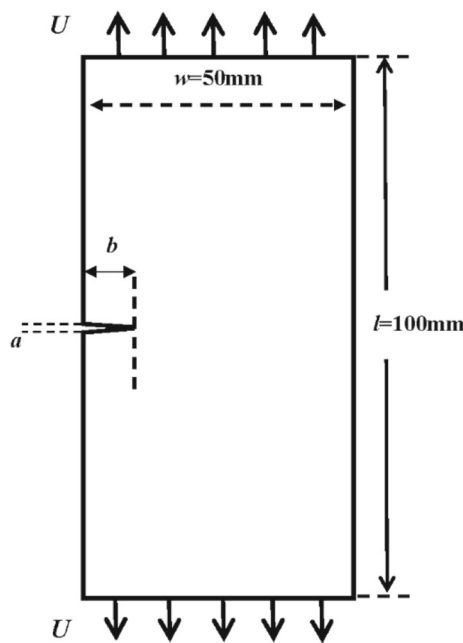
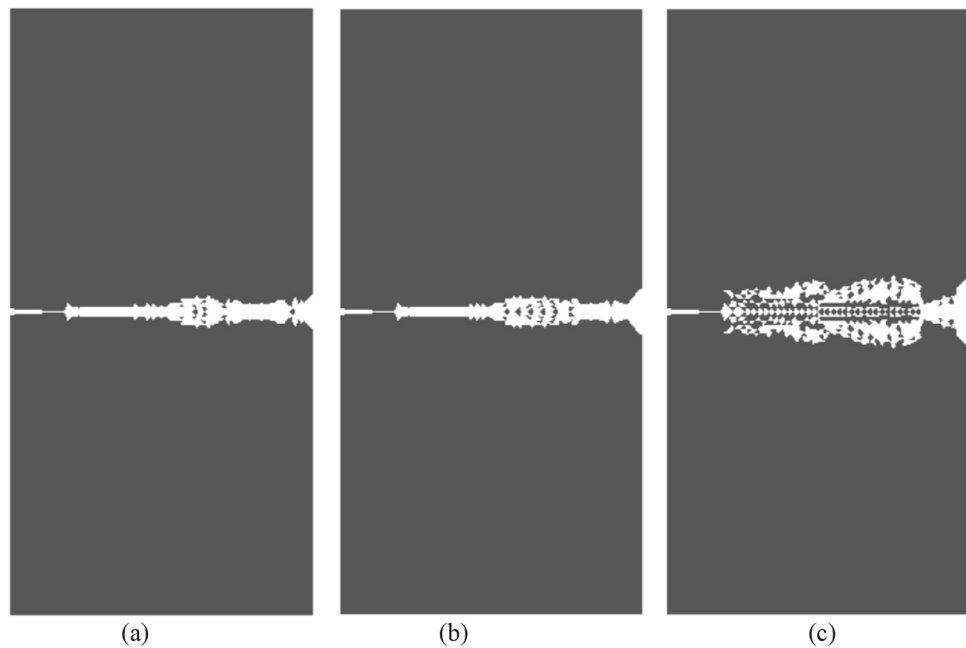


Fig. 15 Geometry of a Mode I cracked plate

3.2.4 Uniaxial tensions of perforated plate

In this subsection, a holed plate with length 0.1 m and width 0.05 m is shown in Fig. 26. The radius of the hole is 0.0015 m located the center of the plate. The Delaunay triangular meshes for the holed plate are represented by $T_h^{a,b,c}$,

Fig. 16 Fracture zones obtained by various fracture criterions for initial length $d = 0.1$ and $\xi = 1e-3$: **a** only with strain term; **b** with energy release rate $G^{(1)}$; **c** with energy release rate $G^{(2)}$



where a , b and c denote the number of nodes on the horizontal, vertical and hole boundaries of the plate. The material constants and displacement increment for each loading step of the plate are also the same with that given in previous Sect. 3.2.2.

Figures 27 and 28 illustrate the fracture zones obtained by the different fracture criterions with various initial crack length $d = 0.1$ and $d = 0.2$ at $\xi = 1e - 3$. It can be seen that the fracture criterions with the second-order strain gradient terms also have a wider fracture zone.

Figure 29 illustrates the fracture zone on the basis of the fracture criterions $G^{(2)}$ with the second-order strain gradient terms for different meshes at $d = 0.2$ and $\xi = 1e - 4$. It is demonstrated that the fracture zone studied using the different meshes is similar. The fracture zone based on the fined meshes $T_h^{200, 100, 300}$ and $T_h^{250, 150, 400}$ has little differences, demonstrating a lower mesh sensitivity for the fracture zone using the fined meshes.

Further, Table 5 lists the fracture strength for different microstructure ξ . Similarly, it can be found that the fracture strength is increased as ξ increasing, and first-order and second-order strain gradients becomes significant for larger ξ . They are also in concordance with the macro properties analysis in Sect. 3.1.

Finally, the fracture strength in comparison to experimental results provided by Li and Zhang [79] is shown in Fig. 30 with calibrated parameters $\xi = 1e - 3$ and initial damage $d = 0.1$. The Young's modulus $E = 3\text{GPa}$, Poisson ratio $\nu = 0.36$ and fracture energy $G_c = 290 \text{ J/m}^2$. The fracture strength for

Fig. 17 Fracture zones obtained by various fracture models for initial length $d = 0.15$ and $\xi = 1e-3$: **a** only with strain term; **b** with energy release rate $G^{(1)}$; **c** with energy release rate $G^{(2)}$

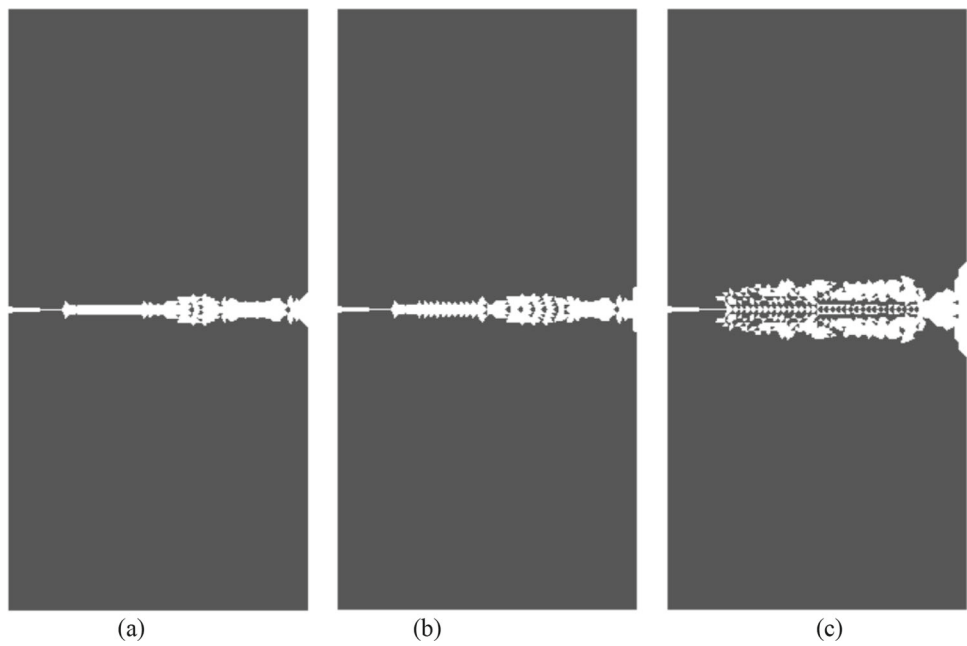


Fig. 18 Fracture zones obtained by various fracture models for initial length $d = 0.2$ and $\xi = 1e-3$: **a** only with strain term; **b** with energy release rate $G^{(1)}$; **c** with energy release rate $G^{(2)}$

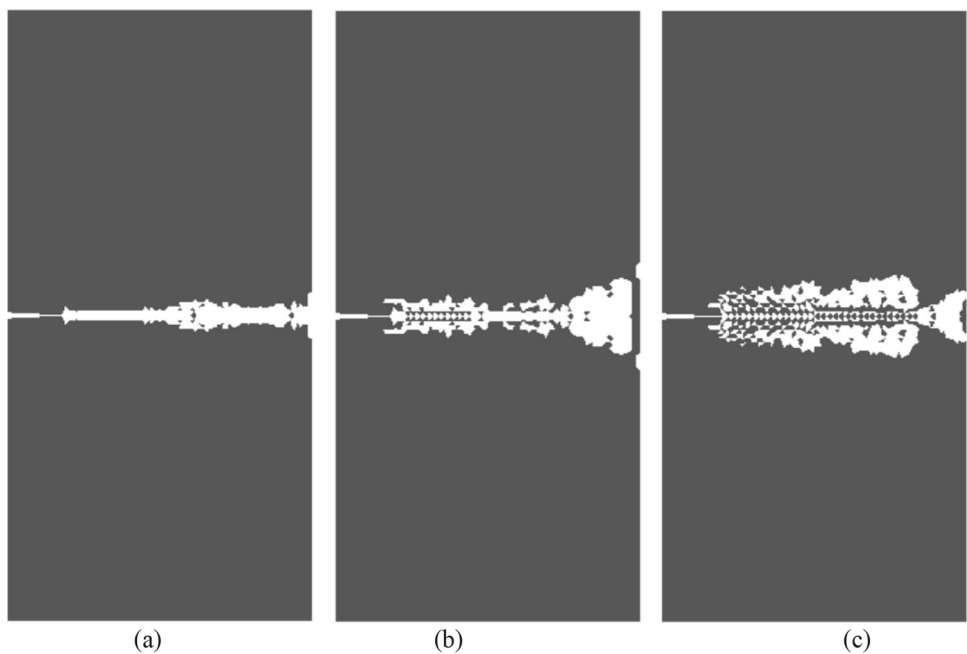


Fig. 19 Fracture zones obtained by various fracture models for initial length $d = 0.1$ and $\xi = 1e-4$: **a** only with strain term; **b** with energy release rate $G^{(1)}$; **c** with energy release rate $G^{(2)}$

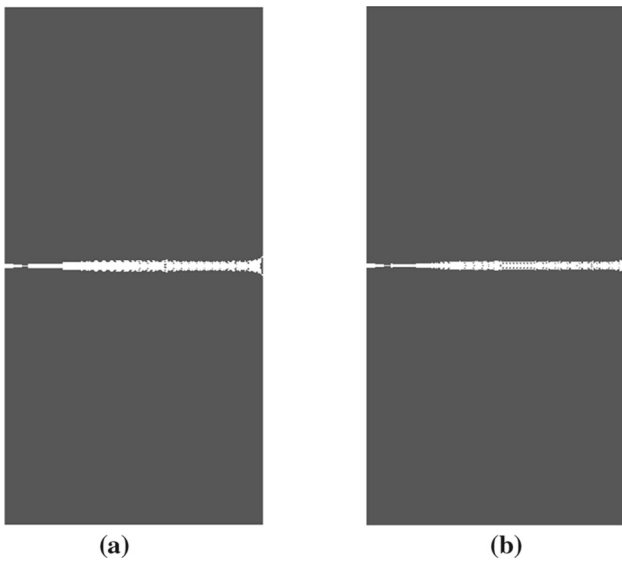
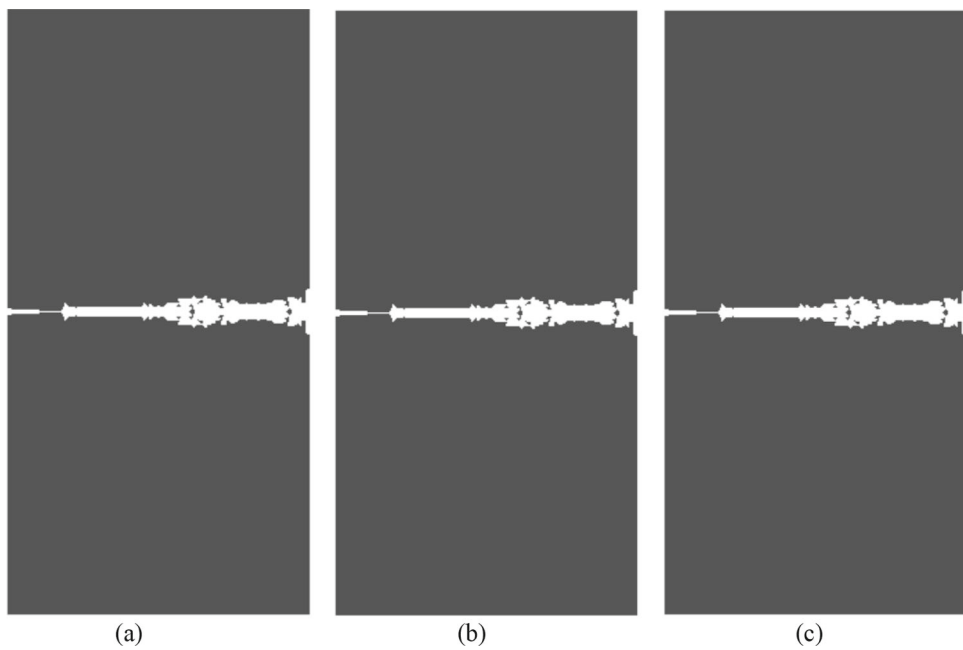


Fig. 20 Fracture zone for different meshes **a** 47,918 elements **b** 107,866 elements

the plate without holes is 72 MPa. As a result, the fracture strength is decreased as the radius r of the hole increasing. The results obtained by the fracture criterions based on $G^{(1)}$ and $G^{(2)}$ agree well with the experimental data as the radius r changing from 0 to 3 mm. Besides, the fracture criterions with strain term will lead to underestimation of the results which are also in accordance with the results proposed in Rao et al. [42].

Table 3 Fracture strength (MPa) for different ξ

	$\xi = 1e-4$	$\xi = 1e-3$	$\xi = 1e-2$
$\sigma_c^{(0)}$	11.1655	3.5334	1.13069
$\sigma_c^{(1)}$	11.1655	3.60407	1.5547
$\sigma_c^{(2)}$	11.166	3.610	1.58263

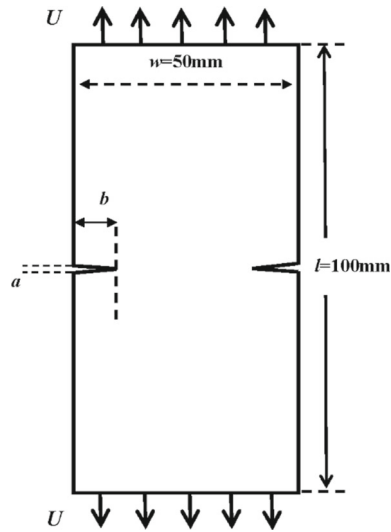


Fig. 21 Geometry of plate with two symmetric V-notch

4 Conclusions

In this work, an effective second-order strain gradient fracture model is developed for the brittle materials with periodic

Fig. 22 Fracture zones obtained by various fracture models for $d = 0.1$ and $\xi = 1e-3$: **a** with strain term; **b** with energy release rate $G^{(1)}$; **c** with energy release rate $G^{(2)}$

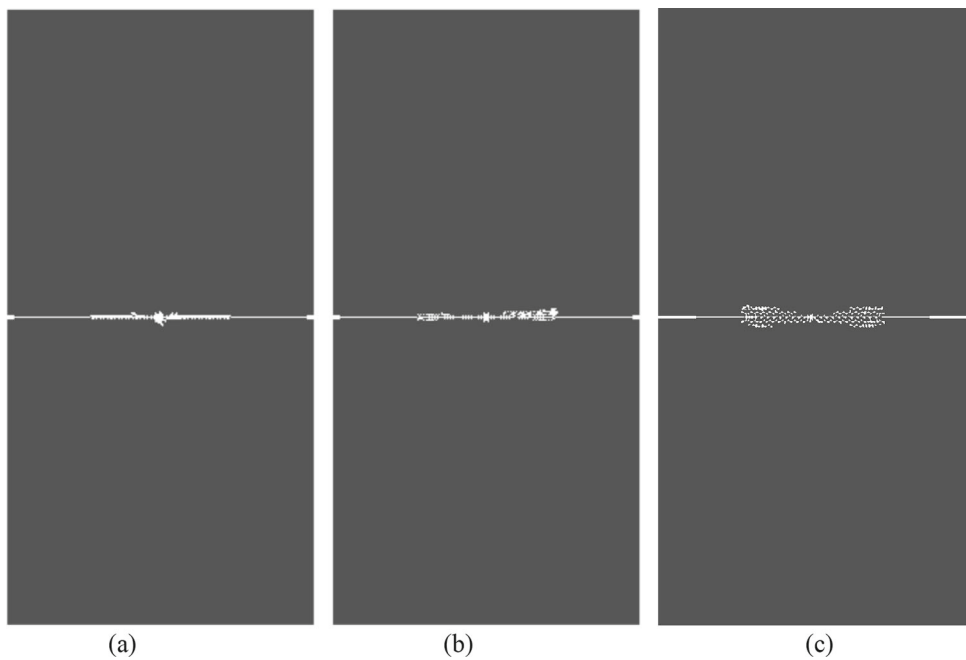


Fig. 23 Fracture zones obtained by various fracture models for $d = 0.1$ and $\xi = 1e-4$: **a** with strain term; **b** with energy release rate $G^{(1)}$; **c** with energy release rate $G^{(2)}$

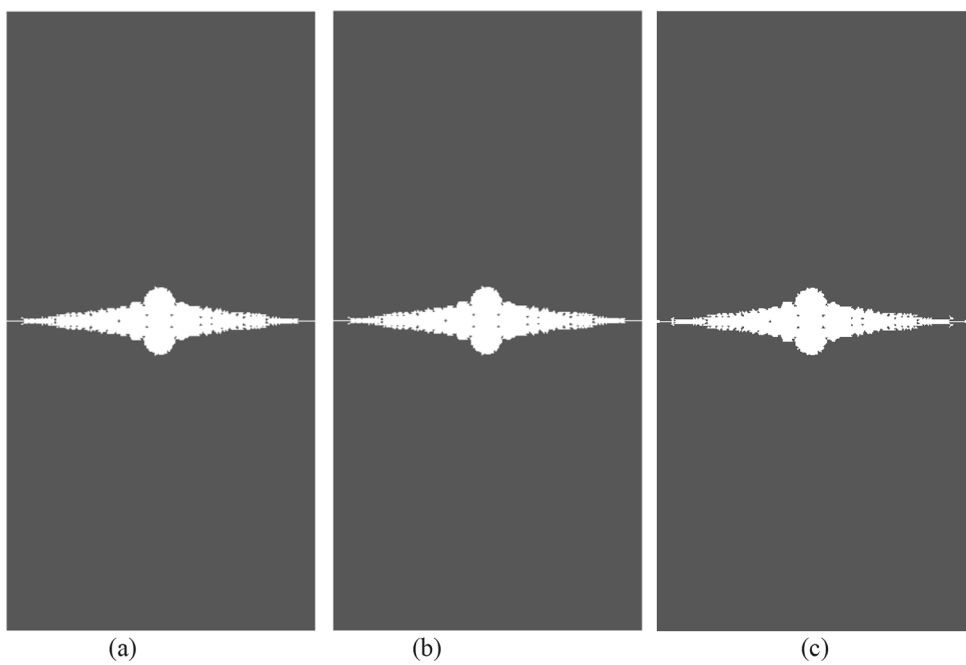


Fig. 24 Fracture zones obtained by the fracture model $G^{(2)}$ for: **a** $d = 0.2$ **b** $d = 0.6$; **c** $d = 0.8$

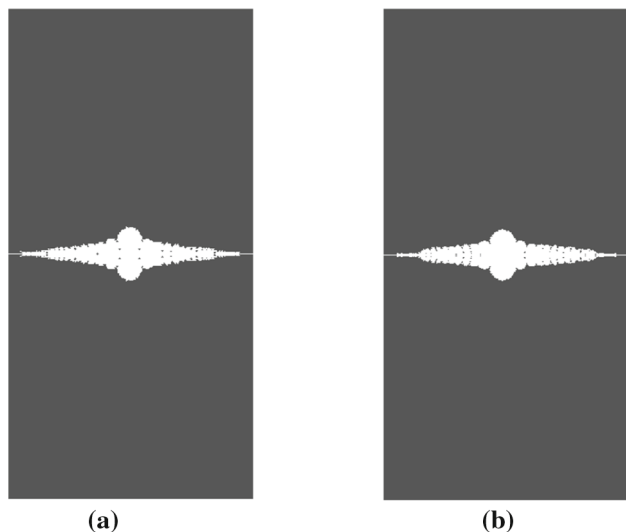
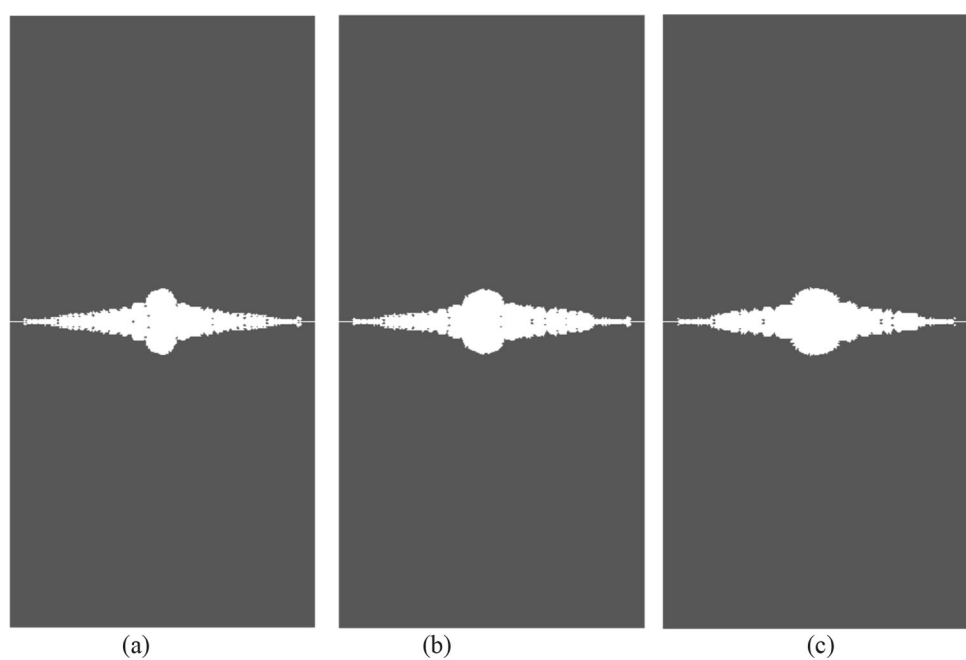


Fig. 25 Fracture zone for different meshes **a** 48,504 elements **b** 94,578 elements

distributions of micro-cracks by a multiscale asymptotic homogenization. The significant features of the fracture models are: (i) the first-order, second-order strain gradient effect

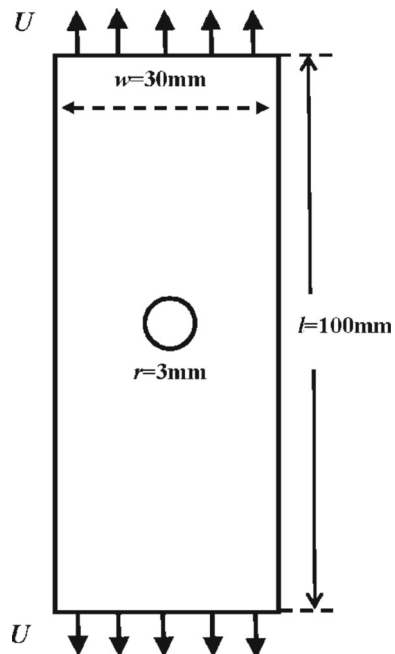


Fig. 26 Geometry of plate with a hole

Table 4 Fracture strength (MPa) for different ξ at $d = 0.1$

	$\xi = 1e-4$	$\xi = 1e-3$	$\xi = 1e-2$
$\sigma_c^{(0)}$	11.1727	3.5911	1.12848
$\sigma_c^{(1)}$	11.1822	3.6162	1.38876
$\sigma_c^{(2)}$	11.183	3.63321	1.44820

Fig. 27 Fracture zones obtained by distinct fracture models for $d = 0.1$ and $\xi = 1e-3$: **a** with the strain term; **b** with energy release rate $G^{(1)}$; **c** with energy release rate $G^{(2)}$

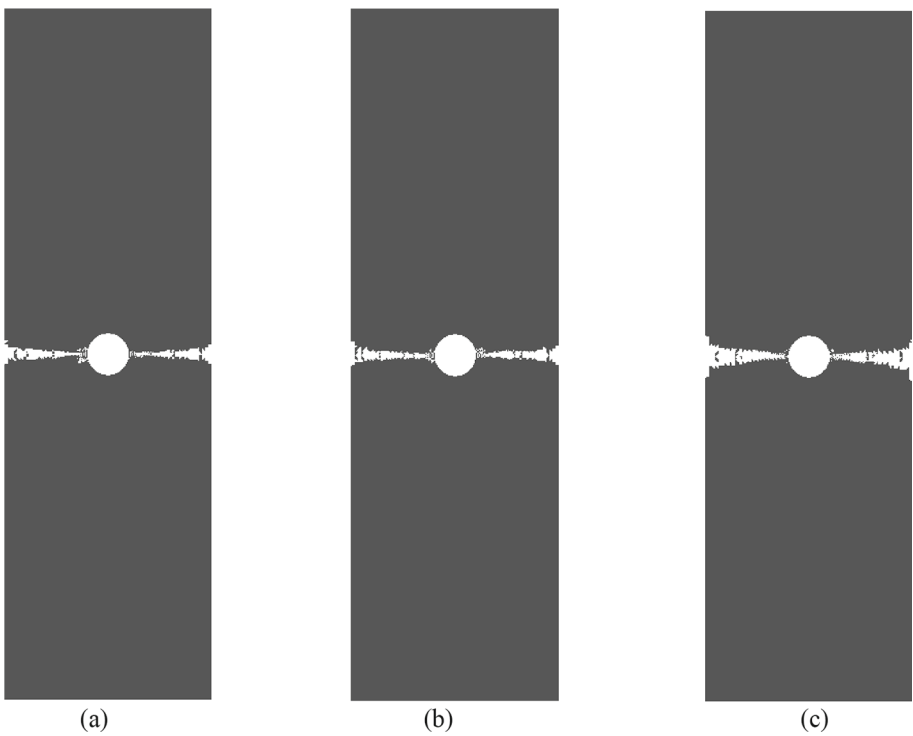


Fig. 28 Fracture zones obtained by distinct fracture models for $d = 0.2$ and $\xi = 1e-3$: **a** with strain term; **b** with energy release rate $G^{(1)}$; **c** with energy release rate $G^{(2)}$

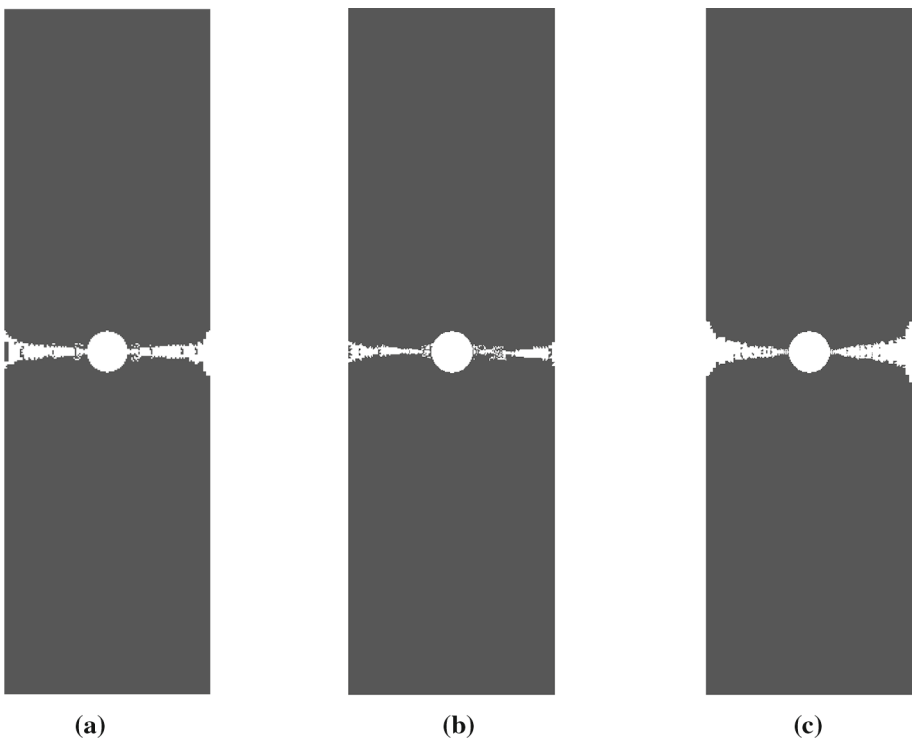


Fig. 29 Fracture zone for three different meshes **a** $T_h^{200, 60, 150}$ **b** $T_h^{200, 100, 300}$ **c** $T_h^{250, 150, 400}$

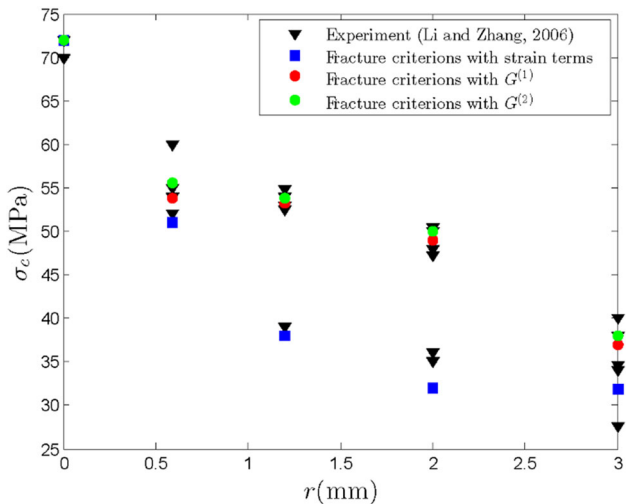
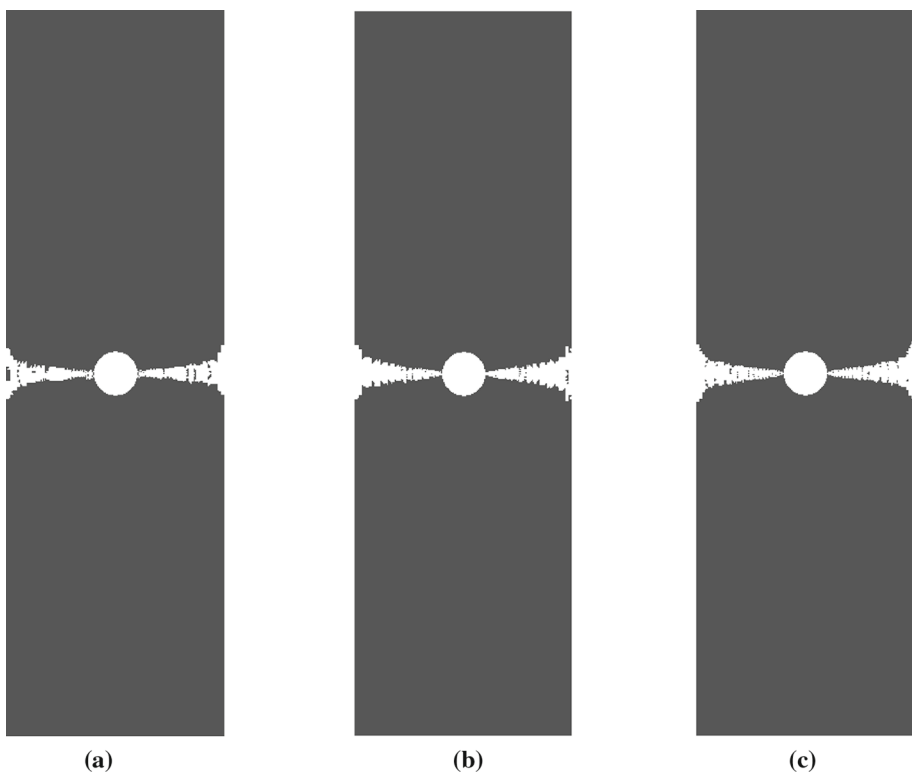


Fig. 30 Comparison of the proposed models and experimental data with $\xi = 1e-3$ for different r

and microstructure size ξ included in the fracture criterion and (ii) the strain energy and the Griffith criterion for micro-crack extensions established by the high-order multiscale asymptotic homogenization. Finally, the effectiveness and accuracy of the proposed approach in comparison to the DNS, experimental data and some typical fracture problems including Mode I crack plate, rectangular plate with two symmetric V-notch and a holed plate are computed by the proposed models. These examples illustrate that the proposed models

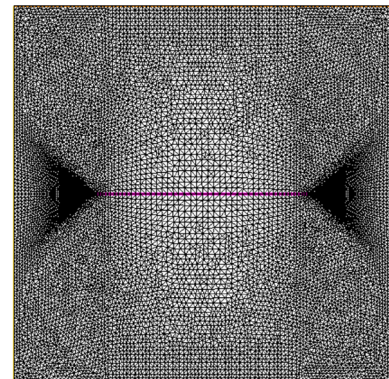


Fig. 31 Refined meshes in unit cell with $d = 0.5$

Table 5 Fracture strength (MPa) for different microstructure ξ

	$\xi = 1e-4$	$\xi = 1e-3$	$\xi = 1e-2$
$\sigma_c^{(0)}$	11.2184	3.55275	1.14605
$\sigma_c^{(1)}$	11.2313	3.58527	1.48986
$\sigma_c^{(2)}$	11.3341	3.66674	1.58893

are effective for evaluating the brittle materials with periodic distributions of micro-cracks. Besides, the fracture zones calculated by the fracture criterions with second-order strain

gradient terms are much more dispersed than that without second-order strain gradient terms for larger ξ ($\xi > 1e-4$).

In addition, the second-order strain gradient fracture model cannot be directly applied to compute the fracture problems of the random heterogeneous structures. Therefore, in the future, this model and relevant numerical techniques will be developed to study the brittle materials with random distributions of micro-cracks. Also, a high-order multiscale simulation will be established to discuss the dynamic micro-crack extension of the brittle materials, and the closures of crack in compressed state should be also investigated.

Acknowledgements The authors would like to acknowledge the research funding from the Excellent Youth Project of Heilongjiang Natural Science Foundation (YQ2021A005).

Appendix A: Theoretical analysis for the multiscale asymptotic expansion

In order to compare $\mathbf{u}_1^\xi(\mathbf{x})$ and $\mathbf{u}_2^\xi(\mathbf{x})$ with the source solutions of (1), we take $\mathbf{u}^\xi(\mathbf{x}) - \mathbf{u}_1^\xi(\mathbf{x})$ into the problem (1) of this work, and has the following equality:

$$\begin{aligned} L_\xi(\mathbf{u}^\xi(\mathbf{x}) - \mathbf{u}_1^\xi(\mathbf{x})) &= f_i(\mathbf{x}) \\ &\times \left[\frac{\partial}{\partial y_j} \left(L_{ijk\alpha_2}(\mathbf{y}) \varphi_m^{\alpha_1 k}(\mathbf{y}) \right) + L_{i\alpha_1 m\alpha_2}(\mathbf{y}) \right. \\ &\quad \left. + L_{i\alpha_1 k j}(\mathbf{y}) \frac{\partial \varphi_m^{\alpha_2 k}(\mathbf{y})}{\partial y_j} \right] \frac{\partial^2 u_k^{(0)}}{\partial x_{\alpha_1} \partial x_{\alpha_2}} + \xi L_{ijkl}(\mathbf{y}) \varphi_m^{\alpha_1 k}(\mathbf{y}) \\ &\quad \frac{\partial^3 u_k^{(0)}}{\partial x_j \partial x_l \partial x_{\alpha_1}} = O(1) \end{aligned} \quad (36)$$

where $L_\xi = -\frac{\partial}{\partial x_j} \left[L_{ijkl}(\frac{\mathbf{x}}{\xi}) \frac{1}{2} \left(\frac{\partial}{\partial x_k} + \frac{\partial}{\partial x_l} \right) \right]$. It can be found that the residual (36) is the order $O(1)$. However, ξ is a fixed parameter rather than tending to zero for practical engineering computation. The error $O(1)$ can be not accepted for scientists who want to accurately obtain the microscopic information of the periodic composites.

Further, taking $\mathbf{u}^\xi(\mathbf{x}) - \mathbf{u}_2^\xi(\mathbf{x})$ into source Eqs. (1) of this work yields to

$$\begin{aligned} L_\xi(\mathbf{u}^\xi(\mathbf{x}) - \mathbf{u}_2^\xi(\mathbf{x})) &= -\frac{\partial}{\partial x_j} \left(L_{ijkl}^\xi(\mathbf{x}) \frac{\partial u_k^\xi(\mathbf{x})}{\partial x_l} \right) \\ &\quad + \frac{\partial}{\partial x_j} \left\{ L_{ijkl}(\mathbf{y}) \frac{\partial}{\partial x_j} \left[\mathbf{u}^{(0)}(\mathbf{x}) + \xi \left(\boldsymbol{\varphi}^{kl}(\mathbf{y}) \varepsilon_{kl}^{(0)}(\mathbf{x}) \right) \right. \right. \\ &\quad \left. \left. + \xi^2 \left(\Phi_p^{kl}(\mathbf{y}) \frac{\partial}{\partial x_p} \varepsilon_{kl}^{(0)}(\mathbf{x}) \right) \right] \right\} = O(\xi), \end{aligned} \quad (37)$$

It is easy to find that the residuals of (37) are the order $O(\xi)$. In other words, the second-order multiscale approximate solutions are equivalent to the solutions of source problem (1) in $O(\xi)$ -order pointwise sense. And, it is important to obtain the accurate solutions of the periodic composites for the actual engineering computations. This is also why we consider the second-order multiscale asymptotic expansion in this work.

Appendix B: Symmetric and anti-symmetric property of first- and second-order cell functions

The micro-cracks of the structure with length l are supposed to be straight, and the cell configurations are symmetric about the middle plane, as shown in Fig. 31. The symmetric and anti-symmetric features of first- and second-order cell functions are shown in Figs. 32 and 33 with normalized micro-crack $d = 0.5$.

The proof of the symmetric and anti-symmetric features for the first-order functions $\varphi_i^{kl}(\mathbf{y})$ can be found in Rao et al. [42] and Cao [80]. Similarly, the symmetry and anti-symmetry for the second-order unit cell functions $\Phi_{ip}^{kl}(\mathbf{y})$ can also obtained Cao [80]. The variational forms of (13) are

$$\begin{aligned} \int_{\Theta_s} & \left(L_{ijk\alpha_2}(\mathbf{y}) \varphi_k^{\alpha_1 m}(\mathbf{y}) + L_{ijkl}(\mathbf{y}) \varepsilon_{ykl}(\Phi_m^{\alpha_1 \alpha_2}(\mathbf{y})) \right) \varepsilon_{yij}(\mathbf{v}) \\ & + (L_{i\alpha_1 m\alpha_2}(\mathbf{y}) + L_{i\alpha_1 k j}(\mathbf{y})) \frac{\partial \varphi_k^{\alpha_2 m}(\mathbf{y})}{\partial y_j} \\ & - \frac{1}{|\Theta_s|} \bar{L}_{i\alpha_1 m\alpha_2} \mathbf{v}_i d\mathbf{y} = 0, \quad \forall \mathbf{v} \in S(\Theta_s) \end{aligned} \quad (38)$$

where $\varepsilon_{ykl}(\mathbf{v}) = \frac{1}{2} (\frac{\partial v_k}{\partial y_l} + \frac{\partial v_l}{\partial y_k})$.

In addition, the function spaces are defined by

$$S(\Theta_s) = \left\{ \mathbf{v} | \mathbf{v} \in \left[H^1(\Theta_s) \right]^2, \mathbf{v} \text{ is periodic in } \Theta_s, \int_{\Theta_s} \mathbf{v} d\mathbf{y} = 0 \right\}$$

where $H^1(\Theta_s)$ represents the Sobolev space [Cao [80]].

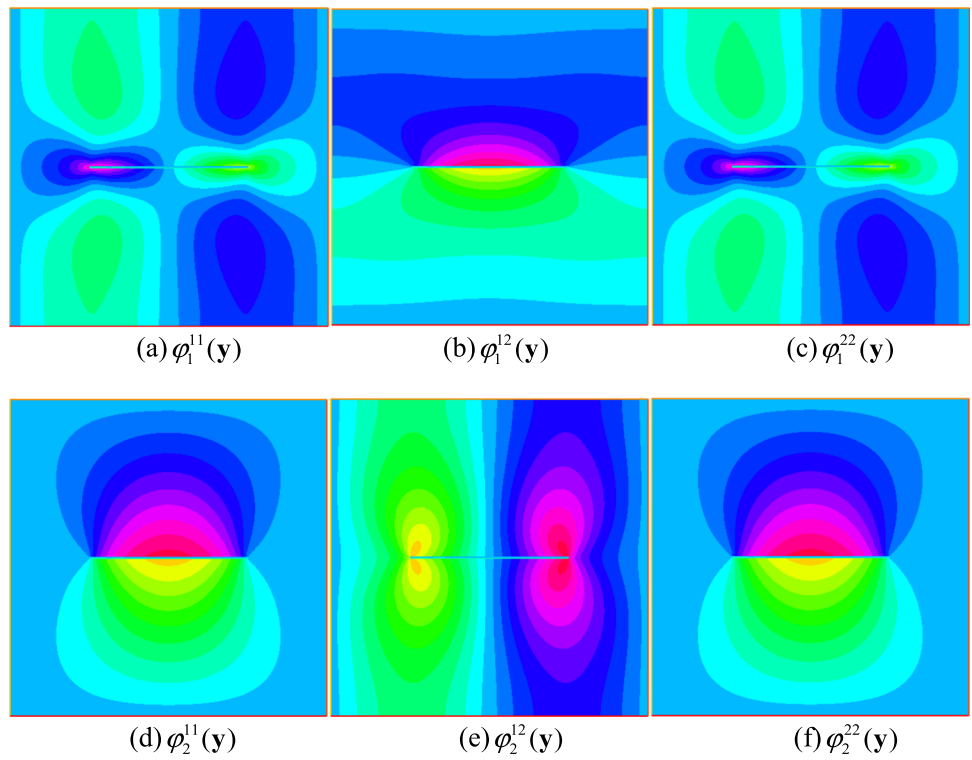
Considering $\Phi_p^{kl}(\mathbf{y})$, and we introduce a vector valued $\overline{\Phi}_1^{11}(y_1, y_2)$ given by

$$\overline{\Phi}_{11}^{11}(y_1, y_2) = \Phi_{11}^{11}(1 - y_1, y_2), \overline{\Phi}_{12}^{11}(y_1, y_2) = -\Phi_{12}^{11}(1 - y_1, y_2).$$

Further, a given test function $\mathbf{v}(y_1, y_2)$ is defined as follows:

$$\bar{\mathbf{v}}_{11}^{11}(y_1, y_2) = \mathbf{v}_{11}^{11}(1 - y_1, y_2), \quad \bar{\mathbf{v}}_{12}^{11}(y_1, y_2) = -\mathbf{v}_{12}^{11}(1 - y_1, y_2)$$

Fig. 32 First-order cell functions $\varphi_i^{kl}(\mathbf{y})$ with $d = 0.5$



Using (38), we have the following equality:

$$\int_{\Theta_s} \left(L_{ijk1}(\mathbf{y})\varphi_k^{11}(\mathbf{y}) + L_{ijkl}(\mathbf{y})\varepsilon_{ykl}(\bar{\Phi}_1^{11}(\mathbf{y})) \right) \varepsilon_{yij}(\bar{\mathbf{v}}) + (L_{i111}(\mathbf{y}) + L_{i1kj}(\mathbf{y}) \frac{\partial \varphi_k^{11}(\mathbf{y})}{\partial y_j} - \frac{1}{|\Theta_s|} \bar{L}_{i111}(\mathbf{y}) \bar{\mathbf{v}}_i) d\mathbf{y} = 0, \quad (39)$$

From (38) and (39), it can be found that $\bar{\Phi}_1^{11}(y_1, y_2)$ and $\Phi_1^{11}(y_1, y_2)$ have the same variational forms. And, the second-order unit cell functions should satisfy that

$$\Phi_{11}^{11}(y_1, y_2) = \bar{\Phi}_{11}^{11}(y_1, y_2) = \Phi_{11}^{11}(1 - y_1, y_2)$$

and.

$$\Phi_{12}^{11}(y_1, y_2) = \bar{\Phi}_{12}^{11}(y_1, y_2) = -\Phi_{12}^{11}(1 - y_1, y_2).$$

Finally, we can obtain the following relations for all the unit cell functions:

$$\begin{aligned} \varphi_1^{11}(y_1, y_2) &= -\varphi_1^{11}(1 - y_1, y_2) = \varphi_1^{11}(y_1, 1 - y_2) \\ \varphi_2^{11}(y_1, y_2) &= -\varphi_2^{11}(y_1, 1 - y_2) = \varphi_2^{11}(1 - y_1, y_2) \\ \varphi_1^{12}(y_1, y_2) &= -\varphi_1^{12}(y_1, 1 - y_2) = \varphi_1^{12}(1 - y_1, y_2) \\ \varphi_2^{12}(y_1, y_2) &= -\varphi_2^{12}(y_1, 1 - y_2) = \varphi_2^{12}(1 - y_1, y_2) \\ \varphi_1^{22}(y_1, y_2) &= -\varphi_1^{22}(1 - y_1, y_2) = \varphi_1^{22}(y_1, 1 - y_2) \\ \varphi_2^{22}(y_1, y_2) &= -\varphi_2^{22}(1 - y_1, y_2) = \varphi_2^{22}(1 - y_1, y_2) \end{aligned} \quad (40)$$

and

$$\begin{aligned} \Phi_{11}^{11}(y_1, y_2) &= \Phi_{11}^{11}(1 - y_1, y_2) = \Phi_{11}^{11}(y_1, 1 - y_2) \\ \Phi_{21}^{11}(y_1, y_2) &= -\Phi_{21}^{11}(y_1, 1 - y_2) = -\Phi_{21}^{11}(1 - y_1, y_2) \\ \Phi_{12}^{11}(y_1, y_2) &= -\Phi_{12}^{11}(y_1, 1 - y_2) = -\Phi_{12}^{11}(1 - y_1, y_2) \\ \Phi_{22}^{11}(y_1, y_2) &= \Phi_{22}^{11}(1 - y_1, y_2) = \Phi_{22}^{11}(y_1, 1 - y_2) \\ \Phi_{11}^{12}(y_1, y_2) &= -\Phi_{11}^{12}(1 - y_1, y_2) = -\Phi_{11}^{12}(y_1, 1 - y_2) \\ \Phi_{21}^{12}(y_1, y_2) &= \Phi_{21}^{12}(1 - y_1, y_2) = \Phi_{21}^{12}(y_1, 1 - y_2) \\ \Phi_{12}^{12}(y_1, y_2) &= \Phi_{12}^{12}(1 - y_1, y_2) = \Phi_{12}^{12}(y_1, 1 - y_2) \\ \Phi_{22}^{12}(y_1, y_2) &= -\Phi_{22}^{12}(1 - y_1, y_2) = -\Phi_{22}^{12}(y_1, 1 - y_2) \\ \Phi_{11}^{22}(y_1, y_2) &= \Phi_{11}^{22}(y_1, 1 - y_2) = \Phi_{11}^{22}(1 - y_1, y_2) \\ \Phi_{21}^{22}(y_1, y_2) &= -\Phi_{21}^{22}(y_1, 1 - y_2) = -\Phi_{21}^{22}(1 - y_1, y_2) \\ \Phi_{12}^{22}(y_1, y_2) &= -\Phi_{12}^{22}(y_1, 1 - y_2) = -\Phi_{12}^{22}(1 - y_1, y_2) \\ \Phi_{22}^{22}(y_1, y_2) &= \Phi_{22}^{22}(y_1, 1 - y_2) = \Phi_{22}^{22}(1 - y_1, y_2) \end{aligned} \quad (41)$$

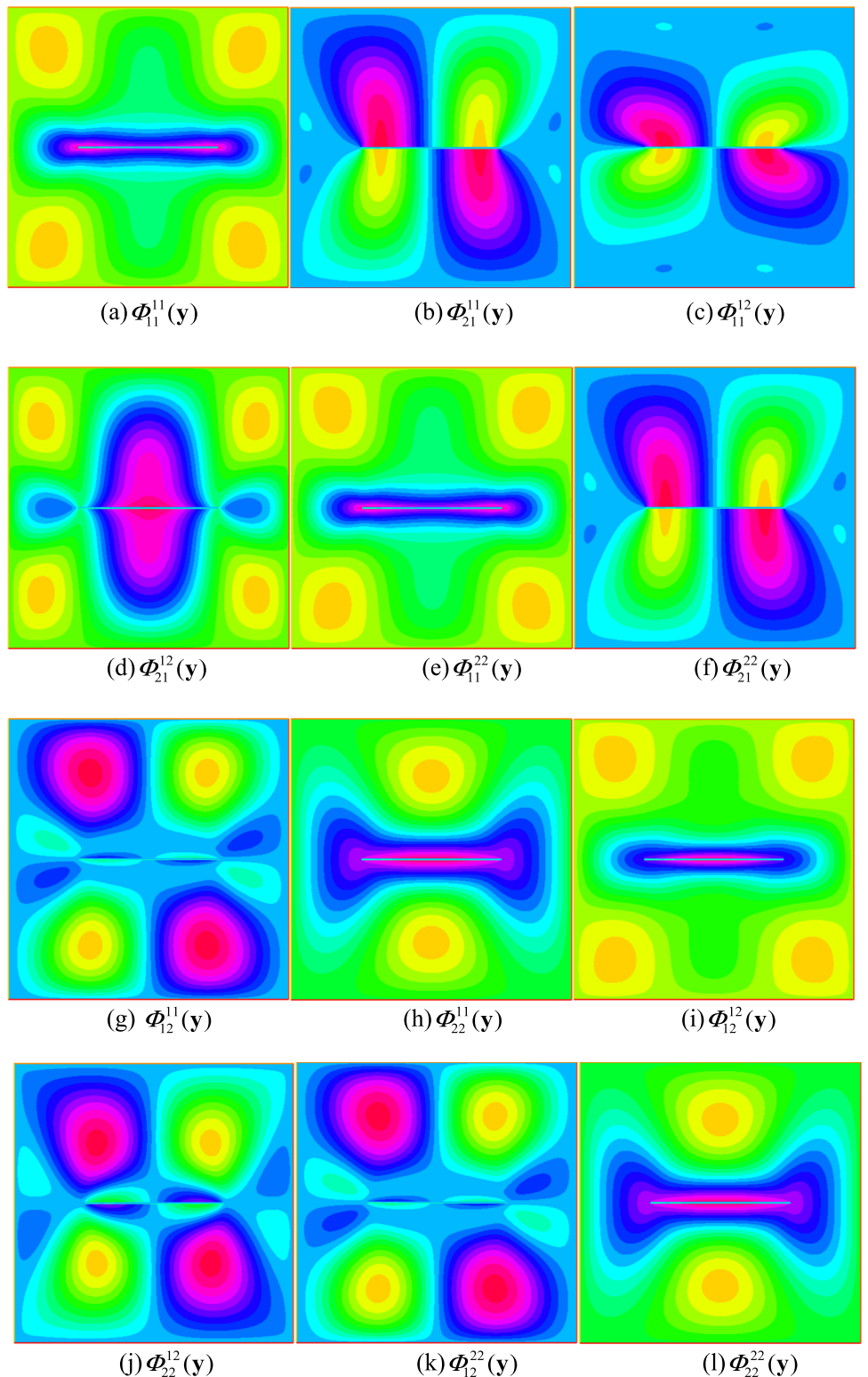
Appendix C: Proof for the equalities (27)

The variational equations of (9) are

$$\int_{\Theta_s} \left(L_{ijkl}(\mathbf{y}) + L_{ijmn}(\mathbf{y})\varepsilon_{ymn}(\varphi^{kl}(\mathbf{y})) \right) \varepsilon_{yij}(\mathbf{v}) d\mathbf{y} = 0, \quad \forall \mathbf{v} \in S(\Theta_s), \quad (42)$$

where $\varepsilon_{ykl}(\mathbf{v}) = \frac{1}{2} \left(\frac{\partial v_k}{\partial y_l} + \frac{\partial v_l}{\partial y_k} \right)$.

Fig. 33 Second-order cell functions $\Phi_{ip}^{kl}(\mathbf{y})$ with $d = 0.5$



Taking $\mathbf{v} = \boldsymbol{\varphi}^{pq}(\mathbf{y})$ in (42), and we have that:

$$\int_{\Theta_s} \left(L_{ijkl}(\mathbf{y}) + L_{ijmn}(\mathbf{y}) \varepsilon_{ymn}(\boldsymbol{\varphi}^{kl}(\mathbf{y})) \right) \varepsilon_{yij}(\boldsymbol{\varphi}^{pq}(\mathbf{y})) d\mathbf{y} = 0. \quad (43)$$

Further, choosing $\mathbf{v} = \Phi_p^{kl}(\mathbf{y})$ for (42) yields to

$$\int_{\Theta_s} \left(L_{ijkl}(\mathbf{y}) + L_{ijmn}(\mathbf{y}) \varepsilon_{ymn}(\boldsymbol{\varphi}^{kl}(\mathbf{y})) \right) \varepsilon_{yij}(\Phi_p^{kl}(\mathbf{y})) d\mathbf{y} = 0. \quad (44)$$

References

1. Francois B, Dascalu C (2010) A two-scale time-dependent damage model based on non-planar growth of micro-cracks. *J Mech Phys Solids* 58:1928–1946
2. Li J (2011) A micromechanics-based strain gradient damage model for fracture prediction of brittle materials - part i: Homogenization methodology and constitutive relations. *Int J Solids Struct* 48(24):3336–3345
3. Li J, Pham T, Abdelmoula R, Song F, Jiang C (2011) A micromechanics-based strain gradient damage model for fracture prediction of brittle materials - part ii: Damage modeling and numerical simulations. *Int J Solids Struct* 48(24):3346–3358
4. Eringen A (1972) Linear theory of nonlocal elasticity and dispersion of plane waves. *Int J Eng Sci* 10(5):425–435
5. Povstenko YZ (1999) The nonlocal theory of elasticity and its applications to the description of defects in solid bodies. *J Math Sci* 97(1):3840–3845
6. Pijaudier-Cabot G, Bazant Z (1987) Nonlocal damage theory. *J Eng Mech* 113:1512–1533
7. Apuzzo A, Barretta R, Canadiga M, Feo L, Luciano R, de Sciarra FM (2017) A closed-form model for torsion of nanobeams with an enhanced nonlocal formulation. *Compos Part B: Eng* 108:315–324
8. Barretta R, Feo L, Luciano R, de Sciarra FM, Penna R (2016) Functionally graded Timoshenko nanobeams: a novel nonlocal gradient formulation. *Compos B Eng* 100:208–219
9. Eringen AC (1983) On differential equations of nonlocal elasticity and solutions of screw dislocation and surface waves. *J Appl Phys* 54(9):4703–4710
10. Aifantis EC (1992) On the role of gradients in the localization of deformation and fracture. *Int J Eng Sci* 30(10):1279–1299
11. Mühlhaus HB, Oka F (1996) Dispersion and wave propagation in discrete and continuous models for granular materials. *Int J Solids Struct* 33(19):2841–2858
12. Ru CQ, Aifantis EC (1993) A simple approach to solve boundary-value problems in gradient elasticity. *Acta Mech* 101(1–4):59–68
13. Aifantis EC (2003) Update on a class of gradient theories. *Mech Mater* 35(3–6):259–280
14. Gutkin MY, Aifantis EC (1999) Dislocations in the theory of gradient elasticity. *Scr Mater* 5(40):559–566
15. Jamalpoor A, Hosseini M (2015) Biaxial buckling analysis of double-orthotropic microplate-systems including in-plane magnetic field based on strain gradient theory. *Compos Part B: Eng* 75:53–64
16. Zhang B, He Y, Liu D, Lei J, Shen L, Wang L (2015) A size-dependent thirdorder shear deformable plate model incorporating strain gradient effects for mechanical analysis of functionally graded circular/annular microplates. *Compos Part B: Eng* 79:553–580
17. Di Paola M, Failla G, Zingales M (2009) Physically-based approach to the mechanics of strong non-local linear elasticity theory. *J Elasticity* 97(2):103–130
18. Di Paola M, Failla G, Pirrotta A, Sofi A, Zingales M (2013) The mechanically based non-local elasticity: an overview of main results and future challenges. *Philos Trans R Soc A* 371(1993):20120433
19. Eringen A, Suhubi E (1964) Nonlinear theory of simple micro-elastic solids-I. *Int J Eng Sci* 2(2):189–203
20. Mindlin R (1964) Micro-structure in linear elasticity. *Arch Ration Mech Anal* 16(1):51–78
21. Toupin R (1962) Elastic materials with couple-stresses. *Arch Ration Mech Anal* 11:385–414
22. Acharya A, Bassani JL (2000) Incompatibility and crystal plasticity. *J Mech Phys Solids* 48:1565–1595
23. Bassani JL, Needleman A, Van der Giessen E (2001) Plastic flow in a composite: a comparison of nonlocal continuum and discrete dislocation predictions. *Int J Solids Struct* 38:833–853
24. Arsenlis A, Parks DM (1999) Crystallographic aspects of geometrically-necessary and statistically-stored dislocation density. *Acta Mater* 47:1597–1611
25. Busso EP, Meissonneir FT, O'Dowd NP (2000) Gradient-dependent deformation of two-phase single crystals. *J Mech Phys Solids* 48:2333–2362
26. Aifantis EC (1984) On the microstructural origin of certain inelastic models. *Trans ASME J Eng Mater Technol* 106:326–330
27. Fleck NA, Hutchinson JW (1993) A phenomenological theory for strain gradient effects in plasticity. *J Mech Phys Solids* 41(12):1825–1857
28. Fleck NA, Hutchinson JW (2001) A reformulation of strain gradient plasticity. *J Mech Phys Solids* 49(10):2245–2271
29. Fleck NA, Hutchinson JW (1997) Strain gradient plasticity. *Adv Appl Mech* 33:295–361
30. Gurtin ME (2002) A gradient theory of single-crystal viscoplasticity that accounts for geometrically necessary dislocations. *J Mech Phys Solids* 50(1):5–32
31. Menzel A (2000) On the continuum formulation of higher gradient plasticity for single and polycrystals. *J Mech Phys Solids* 48(8):1777–1796
32. Gudmundson P (2004) A unified treatment of strain gradient plasticity. *J Mech Phys Solids* 52(6):1379–1406
33. McVeigh C, Liu WK (2008) Linking microstructure and properties through a predictive multiresolution continuum. *Comput Methods Appl Mech Eng* 197(41–42):3268–3290
34. McVeigh C, Vernerey F, Liu WK, Brinson C (2006) Multiresolution analysis for material design. *Comput Methods Appl Mech Eng* 195:5053–5076
35. Vernerey FJ, Liu WK, Moran B (2007) Multi-scale micromorphic theory for hierarchical materials. *J Mech Phys Solids* 55:2603–2651
36. Vernerey FJ et al (2008) A micromorphic model for the multiple scale failure of heterogeneous materials. *J Mech Phys Solids* 56(4):1320–1347
37. Chen J, Wei Y, Huang Y, Hutchinson J, Hwang K (1999) The crack tip fields in strain gradient plasticity: the asymptotic and numerical analyses. *Eng Fract Mech* 64(5):625–648
38. Goutianos S (2011) Mode i and mixed mode crack-tip fields in strain gradient plasticity. *Int J Non-linear Mech* 46(9):1223–1231
39. Jiang H, Huang Y, Zhuang Z, Hwang KC (2001) Fracture in mechanism-based strain gradient plasticity. *J Mech Phys Solids* 49(5):979–993
40. Martinez-Paneda E, Fleck NA (2019) Mode i crack tip fields: strain gradient plasticity theory versus j2 flow theory. *Eur J Mech A/Solids* 75:381–388
41. Peerlings RHJ, De Borst R, Brekelmans WAM, De Vree JHP (1996) Gradient enhanced damage for quasi-brittle materials. *Int J Numer Methods Eng* 39(19):3391–3403
42. Rao YP, Xiang MZ, Cui JZ (2022) A strain gradient brittle fracture model based on two-scale asymptotic analysis. *J Mech Phys Solids* 159:104752
43. Sluys LJ (1992) Wave propagation, localisation and dispersion in softening solids. Dissertation, Delft University of Technology
44. Chang CS, Gao J (1995) Second-gradient constitutive theory for granular material with random packing structure. *Int J Solids Struct* 32(16):2279–2293
45. De Borst R, Mühlhaus HB (1992) Gradient-dependent plasticity: formulation and algorithmic aspects. *Int J Numer Methods Eng* 35:521–539
46. Bacigalupo A, Gambarotta L (2010) Second-order computational homogenization of heterogeneous materials with periodic microstructure. *ZAMM-J Appl Math Mech* 90(10–11):796–811

47. Bacigalupo A, Gambarotta L (2014) Second-gradient homogenized model for wave propagation in heterogeneous periodic media. *Int J Solids Struct* 51(5):1052–1065
48. Goda I, Ganghoffer JF (2016) Construction of first and second order grade anisotropic continuum media for 3D porous and textile composite structures. *Compos Struct* 141:292–327
49. Berkache K, Deogekar S, Goda I, Picu R, Ganghoffer J-F (2017) Construction of second gradient continuum models for random fibrous networks and analysis of size effects. *Compos Struct* 181:347–357
50. Yvonnet J, Auffray N, Monchiet V (2020) Computational second-order homogenization of materials with effective anisotropic strain-gradient behavior. *Int J Solids Struct* 191–192(15):434–448
51. Babu B, Patel BP (2019) A new computationally efficient finite element formulation for nanoplates using second-order strain gradient Kirchhoff's plate theory. *Compos Part B: Eng* 168:302–311
52. Kouznetsova V, Geers M, Brekelmans W (2002) Multi-scale constitutive modeling of heterogeneous materials with gradient enhanced computational homogenization scheme. *Int J Numer Methods Eng* 54:1235–1260
53. Kouznetsova V, Geers M, Brekelmans W (2004) Multi-scale second order computational homogenization of multi-phase materials: a nested finite element solution strategy. *Comput Methods Appl Mech Eng* 193:5525–5550
54. Lesicar T, Tonkovic Z, Soric J (2014) A second-order two-scale homogenization procedure using c1 macrolevel discretization. *Comput Mech* 54(2):425–441
55. Feyeil F (2003) A multilevel finite element method (FE2) to describe the response of highly non-linear structures using generalized continua. *Comput Methods Appl Mech Eng* 192(28–30):3233–3244
56. Forest S (1998) Mechanics of generalized continua: construction by homogenization. *Le J. Phys. IV* 8(PR4):Pr4-39
57. Forest S, Pradel F, Sab K (2001) Asymptotic analysis of heterogeneous cosserat media. *Int J Solids Struct* 38(26–27):4585–4608
58. Gologanu M, Leblond J-B, Perrin G, Devaux J (1997) Recent extensions of Gurson's model for porous ductile metals. In: *Continuum micromechanics*. Springer, pp 61–130
59. Bensoussan A, Lions JL, Papanicolaou G (2011) *Asymptotic analysis for periodic structures*. American Mathematical Society, Rhode Island
60. Jikov VV, Kozlov SM, Oleinik OA (1994) *Homogenization of differential operators and integral functions*. Springer, Berlin
61. Oleinik OA, Shamaev AS, Yosifian GA (1992) *Mathematical problems in elasticity and homogenization*. North-Holland, Amsterdam
62. Allaire G (2003) Homogenization and two-scale convergence. *SIAM J Math Anal* 23(6):1482–1518
63. Hou TY, Wu XH (1997) A multiscale finite element method for elliptic problems in composite materials and porous media. *J Comput Phys* 134:169–189
64. Zhang HW, Wu JK, Fu ZD (2010) Extended multiscale finite element method for elasto-plastic analysis of 2D periodic lattice truss materials. *Comput Mech* 45:623–635
65. Hughes TJR (1995) Multiscale phenomena: Green's functions, the Dirichlet-to-Neumann formulation, subgrid scale models, bubbles and the origins of stabilized methods. *Comput Methods Appl Mech Eng* 127:387–401
66. Zabaras N, Ganapathysubramanian B (2009) A stochastic multi-scale framework for modeling flow through random heterogeneous porous media. *J Comput Phys* 228:591–618
67. Weinan E, Engquist B (2003) The heterogenous multiscale methods. *Commun Math Sci* 1:87–132
68. Yu XG, Cui JZ (2007) The prediction on mechanical properties of 4-step braided composites via two-scale method. *Compos Sci Technol* 67:471–480
69. Yang ZQ, Cui JZ, Sun Y (2016) Transient heat conduction problem with radiation boundary condition of statistically inhomogeneous materials by second-order two-scale method. *Int J Heat Mass Transf* 100:362–377
70. Allaire G, Habibi Z (2013) Second order corrector in the homogenization of a conductive-radiative heat transfer problem. *Discrete Contin Dyn B* 18(1):1–36
71. Bourgat JF (1979) Numerical experiments of the homogenization method for operators with periodic coefficients. In: *Computing Methods in Applied Sciences and Engineering*, Lecture Notes in Math., vol. 704. Springer, Berlin, pp 330–356
72. Gambin B, Kröner E (1989) Higher-order terms in the homogenized stress-strain relation of periodic elastic media. *Phys Stat Sol (b)* 151:513–519
73. Bacigalupo A (2014) Second-order homogenization of periodic materials based on asymptotic approximation of the strain energy: formulation and validity limits. *Meccanica* 49:1407–1425
74. Smyshlyaev VP, Cherednichenko K (2000) On rigorous derivation of strain gradient effects in the overall behaviour of periodic heterogeneous media. *J Mech Phys Solids* 48(6):1325–1357
75. Triantafyllidis N, Bardenhagen S (1996) The influence of scale size on the stability of periodic solids and the role of associated higher order gradient continuum models. *J Mech Phys Solids* 44(11):1891–1928
76. Peerlings RR, Fleck NN (2004) Computational evaluation of strain gradient elasticity constants. *Int J Multiscale Comput Eng* 2(4):599–619
77. Dascalu C, Bilbie G, Agiasofitou EK (2008) Damage and size effects in elastic solids: a homogenization approach. *Int J Solids Struct* 45(2):409–430
78. Keita O, Dascalu C, Francois B (2014) A two-scale model for dynamic damage evolution. *J Mech Phys Solids* 64:170–183
79. Li J, Zhang XB (2006) A criterion study for non-singular stress concentrations in brittle or quasi-brittle materials. *Eng Fact Mech* 73(4):505–523
80. Cao LQ (2006) Multiscale asymptotic expansion and finite element methods for the mixed boundary value problems of second order elliptic equation in perforated domains. *Numer Math* 103:11–45

Publisher's Note Springer Nature remains neutral with regard to jurisdictional claims in published maps and institutional affiliations.

Springer Nature or its licensor (e.g. a society or other partner) holds exclusive rights to this article under a publishing agreement with the author(s) or other rightsholder(s); author self-archiving of the accepted manuscript version of this article is solely governed by the terms of such publishing agreement and applicable law.